Upper limit of the tetrahedral rotation angle and factors affecting octahedral flattening in synthetic and natural 1M polytype C2/m space group micas

Mercier, Patrick; Rancourt, D. G.; Redhammer, G.; Lalonde, A. E.; Robert, J-L.; Berman, R. G.; Kodama, H.

Publisher's version / Version de l'éditeur:
https://doi.org/10.2138/am.2006.1815
Americal Mineralogist, 91, 2006

American Mineralogist, Volume 91, pages 831–849, 2006

Upper limit of the tetrahedral rotation angle and factors affecting octahedral flattening in synthetic and natural 1*M* polytype *C*2/*m* space group micas

Patrick H.J. Mercier,[1] Denis G. Rancourt,[2,*] Guenther J. Redhammer,[3] André E. Lalonde,[4] Jean-Louis Robert,[5] Rob G. Berman,[6] and Hideomi Kodama[7]

[1]Institute for Chemical Process and Environmental Technology, National Research Council Canada, 1200 Montreal Road, Building M-12, Ottawa, Ontario K1A 0R6, Canada
[2]Department of Physics, University of Ottawa, Ottawa, Ontario K1N 6N5, Canada
[3]Institute of Mineralogy, University of Salzburg, A-5020 Salzburg, Austria
[4]Department of Earth Sciences, University of Ottawa, Ottawa, Ontario K1N 6N5, Canada
[5]Centre de Recherches sur la Synthèse et la Chimie des Minéraux (CRSCM), CNRS, 1A, Rue de la Férollerie, F45071 Orléans, Cédex 2, France
[6]Geological Survey of Canada, 601 Booth Street, Ottawa, Ontario K1A 0E8, Canada
[7]ECORC Agriculture and Agri-Food Canada, 960 Carling Avenue, Ottawa, Ontario K1A 0C6, Canada

Abstract

We have used recently developed quantitative crystal chemical models and a simple structural free-energy model to examine and interpret: (1) previously reported powder X-ray diffraction data for several trioctahedral mica solid solution series (64 synthetic powder samples between the Mg, Co, Ni, and Fe end-members, with different degrees of oxidation, vacancy contents, and Al/Si ratios; indexed as 1*M* polytype, space group *C*2/*m*; supplemented here by ^{57}Fe Mössbauer spectroscopy to obtain accurate iron-site populations of $^{IV}Fe^{3+}$, $^{VI}Fe^{3+}$, and $^{VI}Fe^{2+}$), and (2) 175 previously published single-crystal refinements comprising 138 natural and 37 synthetic 1*M* mica samples refined in space group *C*2/*m*. The crystal chemical models were validated by comparisons between predicted and measured relations between structural parameters, and needed model parameters and their uncertainties were extracted, using the single-crystal refinements. Two main results arise. First, an observed limit value of the *b* lattice parameter in certain synthetic solid solution series is shown to correspond to an upper limit value for the tetrahedral rotation angle α of $\alpha_{max} = 9.5°$ for $AlSi_3$ tetrahedral sheets in K-rich micas. This upper limit is also clearly seen in the single-crystal refinement data for those K-rich single-crystals that have near-$AlSi_3$ tetrahedral compositions. We argue that the (tetrahedral sheet composition dependent) upper limit of tetrahedral rotation is an intrinsic property of the tetrahedral sheet (presumably corresponding to an intra-tetrahedral-sheet bond-bending limit) rather than arising either from interactions with the interlayer cations or from an octahedral sheet lateral-contraction limit. Second, we find that, except in the extreme cases where one approaches the lower ($\alpha = 0°$) or upper ($\alpha = \alpha_{max}$) tetrahedral rotation limits, the magnitude of the octahedral flattening angle ψ is predominantly determined by octahedral cation stereo-chemical bonding requirements (and other intra-octahedral-sheet properties such as intra-sheet bond bending and intra-sheet electrostatic forces) rather than arising from tetrahedral-octahedral inter-sheet interactions (as generally argued or assumed). In addition, we corroborate a previously reported difference in the crystal chemical behaviors of trivalent octahedral cation (Fe^{3+}, Al^{3+}) and vacancy-bearing trioctahedral micas relative to samples that contain only divalent octahedral cations (e.g., Fe-Mg, Fe-Ni, Mg-Ni, and Co-Mg synthetic series); their *b* vs. average octahedral metal-oxygen bond-length behaviors are dramatically different, a result that is consistent with our proposed dominant stereo-chemical control of ψ.

Keywords: Crystal chemistry, layer silicate, mica, tetrahedral rotation, inter-sheet matching, octahedral flattening

Introduction

Tetrahedral rotation and octahedral flattening are the two main structural distortion mechanisms which ensure the matching of octahedral and tetrahedral sheets in the mica structure (e.g., Bailey 1984; Brigatti and Guggenheim 2002; Ferraris and Ivaldi 2002) and in layer silicates in general (e.g., Bailey 1988). The degrees of these distortions can be expressed by the tetrahedral rotation angle α and the mean flattening angle ψ of the octahedra (e.g., Donnay et al. 1964a; Hazen and Burnham 1973; Takeda and Morosin 1975). Tetrahedral rotation reduces the lateral extent of tetrahedral sheets, whereas octahedral sheets are laterally expanded by octahedral flattening.

Physical limits to possible mica structures owing to the relative sizes of octahedral and tetrahedral sheets appear to exist. In annite, for example, the ideal end-member stoichiometry

* E-mail: dgr@physics.uottawa.ca

$K(Fe^{2+}_3)(AlSi_3)O_{10}(OH)_2$ is never attained because of mismatch constraints between the larger $^{VI}(Fe^{2+}_3)$ octahedral and smaller $^{IV}(AlSi_3)$ tetrahedral sheets, which require some Fe^{3+} to be present even under highly reducing conditions (Hazen and Wones 1972; Redhammer et al. 1993; Rancourt et al. 1994a, 2001; Mercier et al. 1996, 1999). The latter situation is believed to occur from the geometrical limit of $\alpha = 0°$, which corresponds to the point where a fully expanded (i.e., non-rotated) tetrahedral sheet cannot fit laterally onto an octahedral sheet. At the other extreme, evidence for a possible upper limit on α has been discussed by a few authors (e.g., Hazen and Wones 1978; Redhammer and Roth 2002). In particular, Hewitt and Wones (1975) suggested that an upper limit on α was the reason that Al-substitution is limited in synthetic biotite solid solutions. The idea of geometric structural limits for α (i.e., $0° \le \alpha \le \alpha_{max}$) was used by Hazen (1977) and Hazen and Wones (1978) to study the stability relationships of some end-member trioctahedral micas on a pressure-temperature diagram. On the other hand, Guggenheim et al. (1987) and Russell and Guggenheim (1999) oppose the view that geometric limits in α play a role in the stability of micas.

The origin of octahedral flattening has been analyzed in many structural and crystal chemical studies (e.g., Hazen and Wones 1972; Toraya 1981; Lin and Guggenheim 1983; Bailey 1984a; Weiss et al. 1985, 1992; Alietti et al. 1995, 1997; Brigatti and Davoli 1990; Brigatti and Poppi 1993; Brigatti et al. 1991, 1996a, 1996b, 2000a, 2000b, 2001, 2003a; Cruciani and Zanazzi 1994; Brigatti and Guggenheim 2002; Redhammer and Roth 2002), but so far relatively few researchers have exploited predictions from geometric crystal chemical models to assess octahedral flattening (e.g., Donnay et al. 1964a; Hazen and Wones 1972; Hazen and Burnham 1973; Takeda and Morosin 1975).

In the present paper, we follow an approach based on the geometric crystal chemical models of Mercier et al. (2005a), applied to a large suite of synthetic powder samples previously studied by powder X-ray diffraction (Mercier et al. 2005b) and using previously published single-crystal refinement data. We find that such models provide a powerful framework for analyzing lattice and structural refinement parameters, by allowing clear distinctions to be made between local effects owing to chemical disorder vs. long-range geometric effects that either appear as average network adjustments (e.g., average polyhedral flattening and rotation) or as true geometric limits (i.e., that would require excessive bond stretching or bending). This approach was also applied in a previous paper (Mercier et al. 2005b) to study the nature of octahedral chemical ordering in the same synthetic powder samples and previously published single-crystal refinements studied here.

Throughout the present paper we use the terms *geometric homo-octahedral*, *geometric meso-octahedral*, and *geometric hetero-octahedral* to refer to each of the three octahedral sheet types I, II, and III described by Weiss et al. (1992), which are based on the values of the average cation-anion bond lengths <M1-O>, <M2-O>, and <M3-O> for the three possible octahedral sites: type-I, <M1-O> = <M2-O> = <M3-O>; type-II, any two are equal and the third is different; and type-III, the three average bond lengths are different. When used without the qualifying adjective *geometric*, the terms homo-octahedral, meso-octahedral, and hetero-octahedral refer to the classification based on the symmetry of occupancy of the octahedral sheets [layer symmetries $H(\bar{3})1m$, $P(\bar{3})1m$, and $P(3)12$, respectively] as judged by the refinements of site-specific mean electron counts (Ďurovič 1994; Nespolo and Ďurovič 2002).

Materials and methods

Synthetic powder samples

The 64 synthetic powder samples studied here were described and characterized in detail by Mercier et al. (2005b). Table 1 summarizes the structural formulas for the synthetic powder samples.

Iron site populations from Mössbauer spectroscopy

Transmission ^{57}Fe Mössbauer spectra were collected using a <30 mCi ^{57}Co rhodium-matrix single-line thin source with a constant-acceleration drive over a velocity range of ±4 mm/s. Data were acquired over 1024 channels and folded to give a flat background and a zero-velocity position corresponding to the center shift of metallic α-Fe at room temperature.

Random-orientation powder absorbers were prepared as described previously (Rancourt et al. 1994a, 1994b) using the ideal absorber thickness to obtain the greatest signal-to-noise ratio in the given collection time (Rancourt et al. 1993). Typically, ~25 mg of sample was spread evenly and sandwiched between two waxed paper sheets held with clear tape in aluminum holders with 5/16 inch diameter windows. Because of the small particle size (0.1–20 μm) of synthetic powder samples, this procedure ensured that no texture was present in the absorbers (Rancourt et al. 1994a, 1994b).

Because accurate Fe-site populations were required, all folded raw spectra were corrected for thickness effects as described previously (Rancourt 1989, 1998; Rancourt et al. 1994a, 1994b, 2001). To treat thickness effects properly, each raw spectrum was first fitted with an arbitrary number of Voigt lines to obtain a statistically ideal fit. Intrinsic absorber cross-sections were then extracted from the Voigt fits and used to generate thin-limit spectra (TLS) that are completely corrected for absorber thickness effects, both spectral shape and relative and absolute intensities. Not correcting for thickness effects can cause systematic errors of several percent or more in site populations (e.g., Rancourt et al. 2001).

The only required user-supplied parameter for this exact thickness-effects correction is the average recoilless fraction of the absorber material (Rancourt et al. 1993). A recoilless fraction of $f_a = 0.5$ was obtained from synthetic annite (Royer 1991; Rancourt et al. 1994a) and is the value used for all series, except Fe-Ni GR where $f_a = 0.7$ was used. It is important to note that the thickness-effects correction procedure is not sensitive to the precise value of f_a, i.e., $f_a = 0.5$ or 0.7 gave the same results within experimental error.

In obtaining site populations from Mössbauer spectroscopy, the possibility exists that the site-specific or cation-species-specific recoilless fractions may not be equal for a given sample (Rancourt 1989). In the present work, equal recoilless fractions were assumed for all Fe-sites in a given sample. A complete explanation of the reasons validating this assumption is given in Lalonde et al. (1998) and Rancourt et al. (2001).

The thin-limit spectra were fitted using the Voigt-based quadrupole splitting distribution (QSD) method of Rancourt and Ping (1991) with a 1-1-3 model: one tetrahedral Fe^{3+} site having one Gaussian component in its QSD, an octahedral Fe^{3+}

Table 1. Stoichiometric formulas for the different compositional series of synthetic powder samples studied*

Series name	Stoichiometric formula
Co-Mg JLR	$K(Co_{3-w}Mg_w)(AlSi_3)O_{10}(OH)_2$
Mg-Ni JLR	$K(Mg_{3-w}Ni_w)(AlSi_3)O_{10}(O[H \text{ or } D])_2$
Fe-Mg JLR	$K(Fe^{2+}_{3-w-x-y}Mg_wFe^{3+}_xAl_y)(Al_{1-y}Si_3Fe^{3+}_y)O_{10+x+y}(OH)_{2-x-y}$
Fe-Mg RGBn	"
Fe-Mg RGBr	$K(Fe^{2+}_{3-w-x}Mg_wFe^{3+}_xAl_v)(Al_{1+v}Si_{3-v})O_{10+x}(OH)_{2-x}$
Fe-Ni GR	$K(Fe^{2+}_{3-w-x-y}Ni_wFe^{3+}_xAl_y)(Al_{1-y}Si_3Fe^{3+}_y)O_{10+x+y}(OH)_{2-x-y}$
Ann-oxy-ferrioxy	$K(Fe^{2+}_{3-x-y-3z}Fe^{3+}_{x+2z}\square_zAl_y)(Al_{1-y}Si_3Fe^{3+}_y)O_{10+x+y}(OH)_{2-x-y}$
Ann	$K(Fe^{2+}_{3-x-y}Fe^{3+}_xAl_y)(Al_{1-y}Si_3Fe^{3+}_y)O_{10+x+y}(OH)_{2-x-y}$

* The values of *v*, *w*, *x*, *y*, and *z* were obtained from the nominal compositions of the samples (Mercier et al. 2005b) in combination with the iron site populations (Table 2) in a manner that is explained in the text; the symbol □ designates an octahedral vacancy.

site, also having one Gaussian component, and an octahedral Fe^{2+} site with three Gaussian components in its QSD. Fitting parameters for the room-temperature thin-limit spectra are given in Appendix A.[1] Table 2 lists the $^{[IV]}Fe^{3+}$, $^{[VI]}Fe^{3+}$, and $^{[VI]}Fe^{2+}$ site populations obtained for all iron-bearing samples.

Rancourt and Ping (1991) list all Mössbauer parameter definitions and detailed descriptions of the relevant notation. All steps of the analysis procedure were performed using the Recoil software developed in D.G.R.'s laboratory by K. Lagarec and commercialized by ISA Inc. (www.isapps.ca/recoil).

Treatment of structural refinement and chemical data of the single-crystal samples

We considered structural refinement and chemical data from a compilation of 175 single-crystal refinements of the 1*M* polytype and *C*2/*m* space group recently presented by Mercier et al. (2005b). The structural data used here were re-calculated from unit-cell parameters and atomic coordinates reported by the authors of the original articles. The following site nomenclature is used (site multiplicities are given in parentheses besides each site label): M1(2) and M2(4) indicate octahedral cation sites in *trans*- and *cis*-orientation, respectively; T(8) denotes the tetrahedral cation site; A(2) designates the interlayer cation site; O1(4) and O2(8) represent basal oxygen sites; O3(8) is the apical oxygen site; and O4(4) refers to the site of the (OH), F, Cl, or O octahedral anions.

For the purpose of comparison with the 64 synthetic powder samples, the single-crystal 1*M* samples (Mercier et al. 2005b) were categorized into groups depending on the chemical compositions of the samples. There are four groups of single-crystal samples with compositions similar to our synthetic powder samples: (1) 68 biotite samples close to the annite-phlogopite join with $Al_{apfu} \leq 1.3$, labeled [Ann-Phl] (where X_{apfu} = number of atoms X per formula unit); (2) 42 biotite samples more toward the eastonite-syderophyllite join with $Al_{apfu} > 1.3$, labeled aluminous-[Ann-Phl]; (3) 13 tetra-ferri biotite samples with $^{[IV]}(Fe^{3+})_{apfu} > 0.4$, labeled tetraferri-[Ann-Phl]; and (4) 2 oxy-biotite samples, labeled oxy-Bt. The samples belonging to these four groups are referred to collectively as single-crystal biotite-1*M* samples.

TABLE 2. Iron site populations from Mössbauer spectroscopy (see Appendix A)*

Sample	$^{[IV]}(Fe^{3+})/Fe_{tot}$ (%)	$^{[VI]}(Fe^{3+})/Fe_{tot}$ (%)	$^{[VI]}(Fe^{2+})/Fe_{tot}$ (%)	Fe_{oxide}/Fe_{tot} (%)
Fe-Mg JLR				
$Fe_{0.6}Mg_{2.4}$JLR	not used, Mag	not used, Mag	not used, Mag	not used, Mag
$Fe_{1.2}Mg_{1.8}$JLR	3.69(40)	11.38(46)	84.9(56)	b.d.l.
$Fe_{1.8}Mg_{1.2}$JLR	2.52(32)	14.21(37)	83.26(44)	b.d.l.
$Fe_{2.4}Mg_{0.6}$JLR	4.40(29)	13.11(32)	82.49(39)	b.d.l.
$Fe_{3.0}Mg_{0.0}$JLR	not used, Mag	not used, Mag	not used, Mag	not used, Mag
Fe-Mg RGBn				
$Fe_{0.75}Mg_{2.25}$RGB	3.2(9)	3.5(9)	93.3(12)	b.d.l.
$Fe_{1.5}Mg_{1.5}$RGB	5.08(41)	2.23(49)	92.7(6)	b.d.l.
$Fe_{2.25}Mg_{0.75}$RGB	7.82(17)	2.47(23)	89.71(27)	b.d.l.
$Fe_{3.0}Mg_{0.0}$RGB	6.57(17)	3.08(20)	90.35(26)	b.d.l.
Fe-Mg RGBr				
$Fe_{25}Mg_{75}$Bi33r	b.d.l.	2.42(22)	97.58(22)	b.d.l.
$Fe_{50}Mg_{50}$Bi38r	b.d.l.	4.85(24)	95.15(24)	b.d.l.
$Fe_{75}Mg_{25}$Bi32r	b.d.l.	1.86(16)	98.14(16)	b.d.l.
Fe_{100}Bi35r	b.d.l.	5.26(35)	94.74(35)	b.d.l.
$Fe_{25}Mg_{75}$Bi31r	b.d.l.	10.88(23)	89.12(23)	b.d.l.
$Fe_{75}Mg_{25}$Bi30r	b.d.l.	3.51(11)	96.49(11)	b.d.l.
Fe-Ni GR				
$Fe_{0.2}Ni_{2.8}$GR	23.1(6)	4.1(5)	72.8(5)	b.d.l.
$Fe_{0.6}Ni_{2.4}$GR	11.0(5)	7.6(5)	81.4(7)	b.d.l.
$Fe_{1.0}Ni_{2.0}$GR	7.8(4)	9.3(4)	82.9(5)	b.d.l.
$Fe_{1.4}Ni_{1.6}$GR	5.1(5)	12.1(4)	82.8(6)	b.d.l.
$Fe_{1.8}Ni_{1.2}$GR	5.6(5)	10.0(6)	84.4(4)	b.d.l.
$Fe_{2.2}Ni_{0.8}$GR	5.0(5)	10.6(6)	84.4(7)	b.d.l.
$Fe_{2.6}Ni_{0.4}$GR	4.2(4)	12.1(4)	83.7(6)	b.d.l.
Ann-oxy-ferrioxy†				
IKO-Ann	4.0(2)	7.0(2)	89.0(2)	b.d.l.
EM250	4.22(56)	9.28(63)	86.50(78)	b.d.l.
EM300	5.15(44)	20.78(44)	74.07(53)	b.d.l.
EM350	4.85(50)	47.35(45)	47.80(45)	b.d.l.
EK350	4.14(44)	52.08(38)	43.78(34)	b.d.l.
EK370	not modeled	66.80(15)	30.18(11)	3.02(16)
EM400	not modeled	79.80(31)	13.03(20)	7.17(29)
EM450	not modeled	88.86(38)	b.d.l.	11.14(38)
EM500	not modeled	89.40(32)	b.d.l.	10.60(32)
EM550	not modeled	88.35(35)	b.d.l.	11.65(35)
EM600	not modeled	88.09(34)	b.d.l.	11.91(34)
Annite				
HK-596	4.59(57)	5.71(80)	89.70(93)	b.d.l.
HK-650	5.56(74)	4.7(1.1)	89.8(1.3)	b.d.l.
HK-700	6.99(44)	2.55(59)	90.46(69)	b.d.l.

* Number in parentheses are one-sigma uncertainties estimated with the bootstrap method (see Press et al. 1992 and references therein) implemented in Recoil; samples $Fe_{0.6}Mg_{1.8}$JLR and $Fe_{3.0}Mg_{0.0}$JLR were ignored due to a significant magnetite (Mag) impurity peak seen in the raw Mössbauer spectra; b.d.l. = below detection limit of ~0.2% Fe_{tot}.
† Data taken from Rancourt et al. (2001).

MODEL VALIDATION AND PARAMETER EVALUATION

Validation of geometric crystal chemical models for octahedral and tetrahedral sheets

A sequence of progressively more realistic geometric crystal chemical models for T-O-T layers in micas was described by Mercier et al. (2005a). These models are based on properties of the chemical bonds (bond lengths and bond angles) and can be used to analyze both structural and lattice-parameter refinement data by comparing measured structural properties to predictions based on specific sets of crystal chemical parameters. As these geometric crystal chemical models have not been extensively validated, nor have their limits been systematically examined using a large set of structural refinement results, it was first necessary to do so before applying them to our problem.

An analysis of the structural refinement data for the 175 single crystals (Appendix B) revealed that lattice parameters a and b can be reproduced to within ±0.005 Å from crystal chemical parameters (Table 3), giving the average polyhedral properties of octahedral and tetrahedral sites using the following relationships (Mercier et al. 2005a):

$$a = 3 \cdot d_o \cdot \sin\psi \quad (1a)$$
$$b = 3 \cdot 3^{1/2} \cdot d_o \cdot \sin\psi \quad (1b)$$

$$a = 2\, d_{M1} \sin(\psi_{M1}) + 2\, d_{M2} \sin(\psi_{M2}) \sin[(\pi/6) - \delta_{M2}] \quad (2a)$$
$$b = 3^{1/2}\, d_{M1} \sin(\psi_{M1}) + 2 \cdot 3^{1/2} \cdot d_{M2} \sin(\psi_{M2}) \cos(\delta_{M2}) \quad (2b)$$

$$a = 4 \cdot d_t^{bas} \cdot \sin(\tau_{bas}/2) \cdot \cos\alpha \quad (3a)$$
$$b = 4 \cdot 3^{1/2} \cdot d_t^{bas} \cdot \sin(\tau_{bas}/2) \cdot \cos\alpha \quad (3b)$$

Equations 1, 2, and 3 refer respectively to: (1) a geometric homo-octahedral sheet model where each octahedral site has the same bond length d_o and flattening angle ψ; (2) a geometric meso-octahedral sheet model where d_{M1} and d_{M2} are the site-specific M1 and M2 cation-anion bond lengths, ψ_{M1} and ψ_{M2} are the flattening angles of M1 and M2 octahedra, and δ_{M2} is the counter-rotation angle of the M2 octahedra (the M1 octahedra have zero counter-rotation); and (3) a flat tetrahedral sheet model (i.e., with

[1]Deposit item AM-06-020, Appendix Table A. Deposit items are available two ways: For a paper copy contact the Business Office of the Mineralogical Society of America (see inside front cover of recent issue) for price information. For an electronic copy visit the MSA web site at http://www.minsocam.org, go to the American Mineralogist Contents, find the table of contents for the specific volume/issue wanted, and then click on the deposit link there.

no tetrahedral corrugation or tilting) where each tetrahedron has an equal basal bond length d_t^{bas} for the three T-O_{bas} bonds [i.e., (T-O1) = (T-O2) = (T-O2') = d_t^{bas}], a given basal flattening angle τ_{bas} for the three O_{bas}-T-O_{bas} angles (i.e., $\tau_{O1\text{-}T\text{-}O2} = \tau_{O1\text{-}T\text{-}O2} = \tau_{O2\text{-}T\text{-}O2'} = \tau_{bas}$), and a specified tetrahedral rotation angle α as defined by Donnay et al. (1964a). Table 4 gives a list of all crystal chemical parameters and all equations used to determine the average polyhedral properties of the octahedral and tetrahedral sites.

Based on the extent to which the lateral dimensions of both octahedral and tetrahedral sheets can be reproduced from average polyhedral properties, Equations 1–3 are used below to compare crystal chemical parameters calculated from the lattice parameters of the 64 synthetic powder samples to measured properties obtained from the 175 single-crystal structure refinements.

Obtaining characteristic cation- and coordination-specific bond lengths for mica structures

A key difficulty in testing the models with synthetic powders was to establish characteristic cation- and coordination-specific bond lengths for these structures. This was done (Appendix C) by comparing the bond-length data obtained from the 175 single-crystal refinements to the bond distances obtained using three readily available ways of predicting the bond length of a given cation in a specific coordination: (1) the tables of ionic radii given by Shannon (1976); (2) the bond-valence method of Brown and Altermatt (1985); and (3) the cation-specific octahedral and tetrahedral bond lengths specific to layer silicates given by Weiss et al. (1992). The resulting cation-specific octahedral and tetrahedral bond lengths used in this work are given in Table 4.

For a given synthetic powder sample it, was then possible to obtain a calculated mean octahedral bond length, <M-O>$_{calc}$, and a mean basal tetrahedral bond length, <T-O_{bas}>$_{calc}$, using the following relationships:

$$\langle \text{M-O} \rangle_{calc} = \Sigma_i \, x_i \cdot d_o(\text{M}_i) \quad (4a)$$

$$\langle \text{T-O}_{bas} \rangle_{calc} = \Sigma_i \, x_i \cdot d_t^{bas}(\text{T}_i) \quad (4b)$$

where (1) x_i represents the atomic fraction of cation i contained in the octahedral or tetrahedral sites, and (2) $d_o(M_i)$ and $d_t^{bas}(T_i)$ refer to the characteristic cation-specific octahedral and tetrahedral basal bond lengths specified in Table 4. In turn, values of <M-O>$_{calc}$ and <T-O_{bas}>$_{calc}$ were used to obtain various crystal chemical parameters (described below) from the lattice parameters of the 64 synthetic powders.

TABLE 3. Summary of crystal chemical parameters and equations used to determine the average polyhedral properties of octahedral and tetrahedral sites*

Parameter	Equations used
<M1-O>	= 1/3·[2·(M1-O3) + (M1-O4)]
<M2-O>	= 1/3·[(M2-O3) + (M2-O3′) + (M2-O4)]
<M-O>	= 1/3·[<M1-O> + 2·<M2-O>]
ψ_{M1}	= arccos[h_o/(2·<M1-O>)] where: h_o = 2 c sin(β) [1/2 – (O4z + 2·O3z)/3]
ψ_{M2}	= arccos[h_o/(2·<M2-O>)]
<ψ>	= 1/3·[ψ_{M1} + 2·ψ_{M2}]
δ_{M2}	= $\lvert(\theta_2 + \theta_3) - \theta_1\rvert$/3
<T-O_{bas}>	= 1/3·[(T-O1) + (T-O2) + (T-O2′)]
<τ_{bas}>	= 1/3·[$\tau_{O1\text{-}T\text{-}O2}$ + $\tau_{O1\text{-}T\text{-}O2'}$ + $\tau_{O2\text{-}T\text{-}O2'}$]
α	= 1/6· $\Sigma_{i=1}^{6} \lvert 120° - \phi_i \rvert$

* The symbols (M1-O3), (M1-O4), (M2-O3), (M2-O3'), and (M2-O4) refer to the individual bond lengths occuring in M1 and M2 sites; h_o is the octahedral sheet height; c and β are the monoclinic lattice parameters defining the direction along which the T-O-T layers stack; O3z and O4z are the z fractional atomic coordinates of O3 and O4 sites tabulated in Mercier et (2005b); θ_1, θ_2, and θ_3 are defined in Figure 4 of Mercier et al. (2005b); (T-O1), (T-O2), and (T-O2') are the three T-O_{bas} bond lengths in a given tetrahedron; $\tau_{O1\text{-}T\text{-}O2}$, $\tau_{O1\text{-}T\text{-}O2'}$, and $\tau_{O2\text{-}T\text{-}O2'}$ are the three O_{bas}-T-O_{bas} bond angles in a given tetrahedron; ϕ_i is one of the six distinct crytallographic angles between basal edges of neighboring tetrahedra articulated in the tetrahedral sheets of a 1M polytype $C2/m$ space group structure.

FACTORS AFFECTING OCTAHEDRAL FLATTENING

The vast majority (153 out of 175) of the mica single crystals with 1M polytype and $C2/m$ space group considered here have <M1-O> > <M2-O> and $\psi_{M1} > \psi_{M2}$ (Mercier et al. 2005b). This has been described as the "normal" ordering pattern (e.g., Toraya 1981; Bailey 1984a; Guggenheim 1984), where enlargement of M1 with respect to M2 is believed to be caused by partitioning of high-charge, smaller cations into M2, whereas low-charge, larger cations and vacancies tend to occupy M1. This mode of ordering is consistent with the propositions of Hazen and Wones (1972), who suggested that octahedral flattening is primarily a function of the mean cation radius <R> inside an octahedron, where <R> is obtained using the cation-specific radii of Shannon (1976). Lin and Guggenheim (1983) argued that the flattening of each octahedral cationic site in an octahedral sheet is mainly dependent on the field strengths of the neighboring atoms, where the field strength of an individual atom is equal to its valence divided by its mean cation radius. Alternatively, Weiss et al. (1985) asserted that the flattening ψ and counter-rotation δ angles of any particular octahedron in a sheet are related to interactions in the whole sheet rather than in the particular octahedron alone. Tetrahedral-to-octahedral sheet mismatch is also believed to play a role in determining the magnitude of the flattening angles in a given mica (e.g., Toraya 1981; Lin and Guggenheim 1983).

In a previous paper (Mercier et al. 2005b) it was shown that the 64 synthetic powder samples are geometric homo-octahedral structures with random octahedral occupations, where all octahedral sites have the same flattening angle. By contrast, the 175 single-crystal 1M mica samples have various degrees of chemical order that create geometric meso-octahedral structures with differently sized M1 and M2 octahedral sites. For the single

TABLE 4. Cation- and coordination-specific bond lengths (see Appendix C)

Cation-specific octahedral bond lengths (Å)				
M cation	Weiss et al. (1992)	Brown and Altermatt (1985)	Shannon (1976)	This work
Ni^{2+}	–	2.060	2.057	2.0617(25)
Mg^{2+}	2.083	2.099	2.087	2.0759(22)
Co^{2+}	–	2.098	2.112	2.0876(25)
Fe^{2+}	2.110	2.140	2.147	2.126(11)
Fe^{3+}	2.053	2.015	2.012	2.0263(71)
Al^{3+}	1.919	1.907	1.902	1.945(22)
Ti^{4+}	2.073	1.965	1.972	–
Li^{1+}	2.107	2.129	2.127	–
Cr^{3+}	2.040	1.980	1.982	–
Mn^{3+}	–	2.016	2.012	–
Mn^{2+}	2.140	2.196	2.197	–
Vacancy	2.210	–	–	2.210

Cation-specific basal tetrahedral bond lengths (Å)

	This work		Shannon (1976)	This work
T-sheet	d_t^{bas} or T-O_{bas}	T cation	($^{[4]}$T-$^{[3]}$O)-($^{[4]}$T-$^{[4]}$O)	$d_t^{bas}(T_i)$
$^{[IV]}(Al_{1.1}Si_{2.9})$	1.659	Si^{4+}	1.62–1.64	1.610
$^{[IV]}(FeSi_3)$	1.682	Al^{3+}	1.75–1.77	1.787
$^{[IV]}(Al_{2.8}Si_{1.2})$	1.734	Fe^{3+}	1.85–1.87	1.897

crystals, Mercier et al. (2005b) showed that the counter-rotation angle of the M2 site, δ_{M2}, exactly (within expected experimental error) follows model geometric meso-octahedral sheet predictions given by the following relationship:

$$[d_{M1}^2 - d_{M2}^2] / a^2 = (1/3) \cdot \{\sin^2[(\pi/6) + \delta_{M2}] - 1/4\} / \{\sin^2[(2\pi/3) - \delta_{M2}]\} \quad (5)$$

The counter-rotation angle δ_{M2} is therefore well suited to quantify the degree of octahedral chemical order in a mica with 1*M* polytype and *C*2/*m* space group (i.e., the difference between d_{M1} and d_{M2}), and will be used below as such in assessing octahedral flattening from the perspective of the geometric crystal chemical models.

b as a function of the average octahedral bond length

Figure 1 shows *b* vs. the mean octahedral bond length <M-O>$_{calc}$ (Eq. 4a) determined for various solid solution series of synthetic powder samples. Similarly, Figure 2 displays *b* as a function of the average octahedral sheet bond length <M-O> (Table 3) for the various groups of single-crystal biotite-1*M* samples. Some octahedral flattening ψ = constant (solid lines) predictions made via Equation 1, which are valid for both geometric homo-octahedral and geometric meso-octahedral model octahedral sheets, are shown as references in these figures. For a given synthetic powder sample, <M-O>$_{calc}$ is obtained from Equation 4a using the cation-specific octahedral bond lengths (Table 4 and Appendix C), the nominal composition of the sample (Mercier et al. 2005b), and the measured ferric and ferrous iron site populations obtained by Mössbauer spectroscopy (Table 2 and Appendix A), assuming that any amounts of tetrahedral ferric iron $^{[IV]}Fe^{3+}$ occur through Al/Fe exchange between octahedral and tetrahedral sheets (i.e., via the intra-crystalline reaction: $^{[IV]}Al^{3+} + {}^{[VI]}Fe^{3+} \leftrightarrow {}^{[VI]}Al^{3+} + {}^{[IV]}Fe^{3+}$). In the case of the annite-oxyannite-ferrioxyannite series (Ann-oxy-ferrioxy), following Rancourt et al. (2001), annite-oxyannite ($Fe^{2+} + OH^- \leftrightarrow Fe^{3+} + O^{2-} + H\nearrow$) and oxyannite-ferrioxyannite ($3\,Fe^{2+} \leftrightarrow 2\,Fe^{3+} + {}^{[VI]}\square + Fe\nearrow$) stoichiometries were assumed at $T_{TR} \leq 350$ °C and $T_{TR} \geq 370$ °C, respectively (Fig. 1a).

As illustrated in Figure 1b, the distinct crystal chemical behaviors of the "divalent" (Co-Mg JLR, Mg-Ni JLR, Fe-MgJLR, Fe-Mg RGBn, and Fe-Ni GR) and "trivalent" and/or vacancy-bearing (Ann-oxy-ferrioxy and Fe-Mg RGBr) synthetic solid-solution series, shown in Figure 1a and first described by Rancourt et al. (2001), do not depend on the particular values of cation-specific octahedral bond lengths that are assumed. That is, the *difference* in crystal chemical behavior of these two groups of samples (Fig.1a) survives any particular assumed values for the octahedral bond lengths. The error bars displayed in Figure 1b represent the maximum variations in <M-O>$_{calc}$ values obtained for each sample using the individual 1σ errors of the

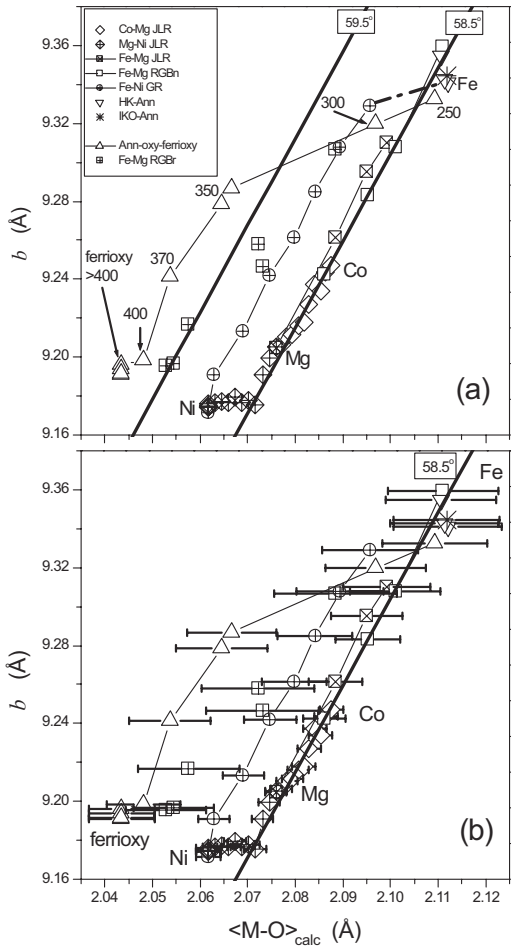

FIGURE 1. (**a**) Lattice parameter *b* vs. the mean octahedral bond length <M-O>$_{calc}$ (Eq. 4a) determined for the synthetic powder samples. (**b**) Plot of *b* vs. <M-O>$_{calc}$ showing the maximum variations of <M-O>$_{calc}$ values (displayed *x*-axis error bars), that were obtained using the individual 1σ errors of the cation-specific $d_o(M_i)$ values (Table 4, Appendix C). The solid lines correspond ψ = constant predictions (validated in Appendix B) made via Equation 1.

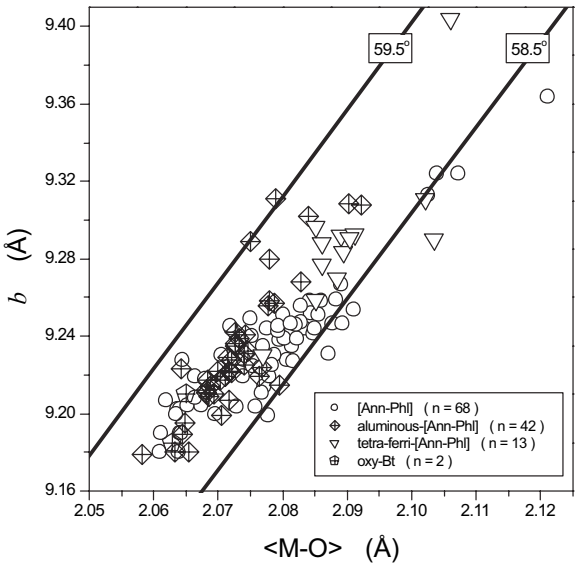

FIGURE 2. Lattice parameter *b* vs. <M-O> (Table 3) observed for the various groups of single-crystal biotite-1*M* samples. The solid lines correspond ψ = constant predictions (validated in Appendix B) made via Equation 1.

cation-specific $d_o(M_i)$ values given in Table 4. Moreover, the break observed in the behavior of the Ann-oxy-ferrioxy series between T_{TR} = 350 and 370 °C (Fig. 1a) occurs regardless of the stoichiometries assumed for these samples. That is, any combination of the oxybiotite reaction ($Fe^{2+} + OH^- \leftrightarrow Fe^{3+} + O^{2-} + H\nearrow$) and the Fe vacancy substitution ($3\ Fe^{2+} \leftrightarrow 2\ Fe^{3+} + {}^{[6]}\square + Fe\nearrow$) gives a discontinuity such as the one exhibited in Figure 1a.

The break in *b* observed for the Mg-Ni JLR series (Fig. 1) corresponds to the upper limit of the tetrahedral rotation angle α (see below). Chemical substitution of a smaller Ni^{2+} cation for a larger Mg^{2+} cation in the octahedral sheets at a constant $^{[IV]}(AlSi_3)$ tetrahedral composition should lead to progressive increase in the dimensional tetrahedral-to-octahedral sheet misfit so that α becomes larger as the average octahedral bond length is reduced. Given that the behavior of *b* is real, therefore, this constitutes direct experimental evidence of the existence of a lower limit of lateral extension concurrent with an upper limit of α-rotation for a given tetrahedral composition.

In Figure 1a, the positions of the solid-solution lines of those nominally divalent series that contain Fe move progressively from ψ = 58.5° to higher ψ = constant predictions as the Fe^{3+}/Fe^{2+} ratio of the given series increases (Table 2), in the sequence Fe-Mg RGBn < Fe-Mg JLR < Fe-Ni GR. This is further illustrated in Figure 3a, where the calculated flattening angles ψ_{calc} (obtained via Eq. 1) are plotted as a function of $<M\text{-}O>_{calc}$. Note, however, that the slopes of the *b* vs. $<M\text{-}O>_{calc}$ lines for the different synthetic solid solution series (Fig. 1a) depend strongly on the particular values of cation-specific octahedral bond lengths $d_o(M_i)$ assumed, within the range given by the individual 1σ errors (Table 4). That is, the ψ = constant behaviors shown in Figure 1a may not be real (i.e., are not robust), however, the series-to-series increases in ψ with increasing Fe^{3+}/Fe^{2+} ratio are real.

Figures 2 and 3b show that in the single-crystal biotite-1*M* samples, the average flattening angle <ψ> (Table 3) decreases with increasing average octahedral bond length <M-O>. Note also that the range of <ψ> values observed for the single-crystal biotite-1*M* samples is closely delimited by the values of ψ_{calc} that were obtained for the Mg-Ni JLR, Co-Mg JLR, and Ann-oxy-ferrioxy solid solution series. Given that geometric homo- and meso-octahedral sheet models (Eqs. 1 and 2) both predict the same constant flattening-angle lines on a graph of *b* vs. <M-O> and that both these models accurately predict *b* to within ±0.005 Å (Appendix B), this means that the scatter observed in Figures 2 and 3b is related to the different (sample to sample) average octahedral flattening angles <ψ> that occur in the biotite-1*M* single crystals (the origin of this scatter is analyzed below).

We conclude that different samples that have the same average octahedral sheet bond length <M-O> can have significantly different average octahedral flattening <ψ> angles, as predominantly determined by their trivalent octahedral cation (Fe^{3+}, Al^{3+}) and vacancy contents.

Indeed, trivalent octahedral cation (Fe^{3+}, Al^{3+}) and vacancy-bearing synthetic powder samples give crystal chemical behaviors distinct from those of the divalent cation series, corresponding to larger *b* and ψ_{calc} for given $<M\text{-}O>_{calc}$ values, relative to samples belonging to the divalent synthetic solid series

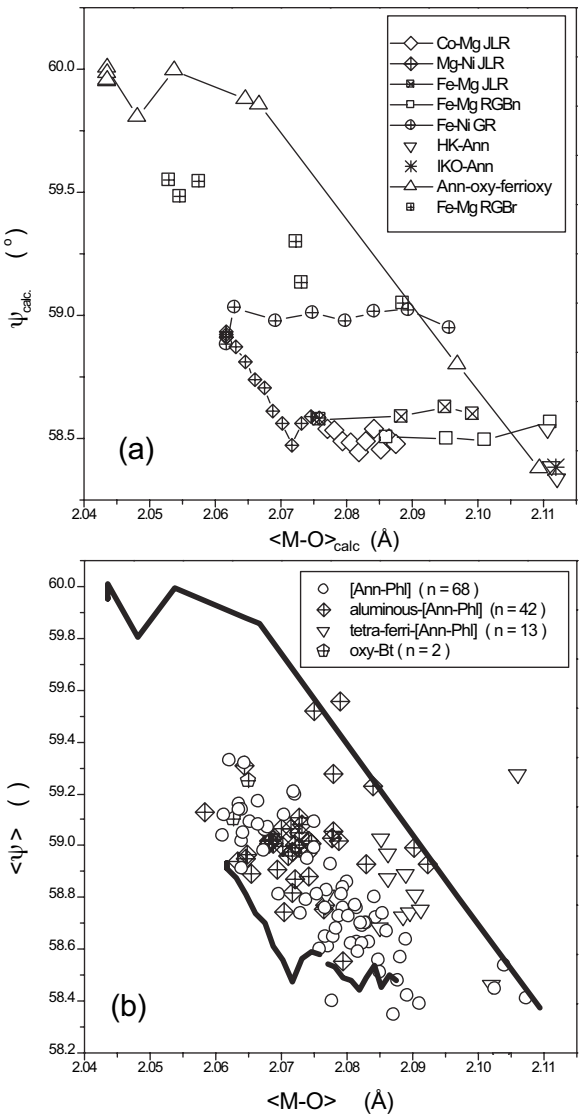

FIGURE 3. (**a**) Plots of ψ_{calc} vs. $<M\text{-}O>_{calc}$ (Eq. 4a) for the synthetic powder samples assuming the cation-specific $d_o(M_i)$ values (Table 4, Appendix C). (**b**) Plot of <ψ> vs. <M-O> (Table 3) for the various groups of single-crystal biotite-1*M* samples. The thick dark lines correspond to ψ_{calc} and $<M\text{-}O>_{calc}$ values obtained for the Mg-Ni JLR, Co-Mg JLR, and Ann-oxy-ferrioxy solid solution series.

(Fe-Mg, Fe-Ni, Mg-Ni, and Co-Mg). The apparent absence of such distinct crystal chemical behaviors between the various groups of single-crystal biotite-1*M* samples (Figs. 2 and 3b) is consistent with these findings, as natural micas most often contain multiple cationic substitutions compared to the simple solid-solution series of the synthetic powder samples. Similar conclusions were reached by previous authors (e.g., Brigatti et al. 1991; Redhammer and Roth 2002; Brigatti and Guggenheim 2002) without *b* vs. <M-O> plots. All these observations (Figs. 1a, 2, and 3) are consistent with the dominant intra-octahedral-sheet (octahedral cation stereo-chemical) control of ψ that we propose below.

Magnitude of octahedral flattening angles vs. M1/M2 chemical ordering

Figure 4 shows the M1/M2 flattening angle tangent ratio, $\tan(\psi_{M1})/\tan(\psi_{M2})$, as a function of the counter-rotation angle δ_{M2} (Table 3). The solid line shown in this Figure corresponds to geometric meso-octahedral model predictions made using the following relationship (Mercier et al. 2005a):

$$\tan(\psi_{M1})/\tan(\psi_{M2}) = 2\cdot\sin[(\pi/6) + \delta_{M2}] \quad (6)$$

In such a representation involving average polyhedral properties of M1 and M2 sites (ψ_{M1}, ψ_{M2}, δ_{M2}), an agreement within expected experimental error is observed between the geometric meso-octahedral sheet model and mica structures with the 1*M* polytype and *C*2/*m* space group. The only exception corresponds to the norrishite sample refined by Tyrna and Guggenheim (1991), which exhibits unusual octahedral site distortions that are presumably related to Jahn-Teller effects (Tyrna and Guggenheim 1991; Brigatti and Guggenheim 2002). This agreement (Fig. 4) represents strong evidence that the flattening angle tangent ratio between M1 and M2 sites directly follows from the degree of octahedral chemical ordering that causes differently sized M1 and M2 octahedral sites in the single crystals (Mercier et al. 2005b).

However, the degree of octahedral chemical order in the single crystals is *not* related to the magnitude of the octahedral flattening angle <ψ>. This is demonstrated in Figure 5, which shows plots of <ψ> as a function of δ_{M2} for the [Ann-Phl], aluminous-[Ann-Phl], and tetraferri-[Ann-Phl] groups of single-crystal biotite-1*M* samples. As indicated by the correlation coefficient (CORR) values, there is no direct relationship between <ψ> and δ_{M2}.

Figure 6 shows plots of ψ_{M1} vs. <M1-O> and ψ_{M2} vs. <M2-O> (Table 3) for the different groups of single-crystal biotite-1*M*

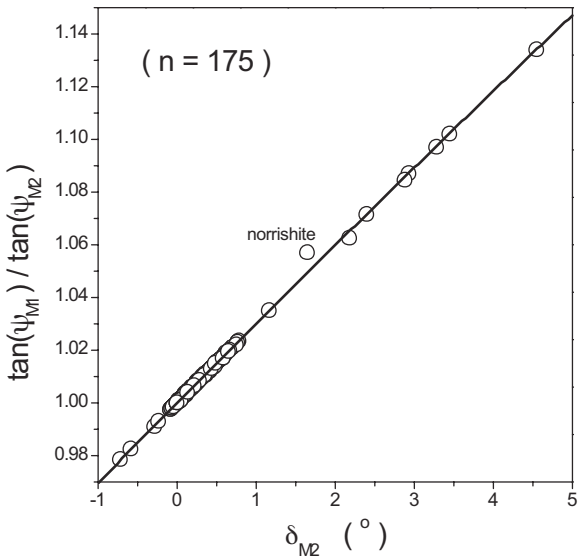

FIGURE 4. Flattening angle tangent ratio $\tan(\psi_{M1})/\tan(\psi_{M2})$ vs. the counter-rotation angle of the M2 site δ_{M2} (Table 3) for the single-crystal 1*M* refinements.

samples. For the [Ann-Phl] and oxy-Bt samples (Figs. 6b and 6d), we note that the individual ψ_{M1} and ψ_{M2} flattening angles decrease as the <M1-O> and <M2-O> bond lengths increase, respectively, but that the correlation is much higher for M2 than for M1. Similar observations have been made elsewhere (Brigatti et al. 1991; Redhammer and Roth 2002). The tetraferri-[Ann-Phl] samples show correlations similar to those found in the [Ann-Phl] and oxy-Bt samples, except for one sample (Figs. 6a and 6c). The aluminous-[Ann-Phl] samples (Figs. 6a and 6c) do not show linear correlations between flattening angles and octahedral cation bond lengths. This is probably related to the large fractions of $^{[VI]}Al^{3+}$ and suggests that octahedral flattening is largely determined by the nature of the octahedral cation.

The above observations (Fig. 6) are consistent with the fact that in model geometric meso-octahedral sheets, the magnitude of the flattening angles need not be related to the degree of octahedral chemical ordering other than through the M1/M2 flattening angle tangent ratio (Eq. 6; Fig. 4). So if there is a simple relation between the bond length and flattening angle for a particular octahedral site, for example a linear correlation such as that observed for the M2 sites of [Ann-Phl] and oxy-Bt single-crystal samples (Fig. 6d), then the lesser degree of correlation obtained for ψ_{M1} vs. <M1-O> (Fig. 6b) is caused by the various degrees of M1/M2 chemical order which occur in the samples. In this way, this also partly contributes to the scatter observed in the plot of *b* vs. <M-O> for the biotite-1*M* single crystals (Fig. 2). Having also shown (Fig. 5) that the average octahedral flattening <ψ> is not related to δ_{M2} (i.e., to the degree of octahedral chemical order; Fig. 4), we conclude that the magnitude of the octahedral flattening is not determined by the degree of M1/M2 chemical ordering that occurs in the sample and that only the M1/M2 flattening angle tangent ratio follows from differently sized M1 and M2 octahedral sites, as predicted in a geometric meso-octahedral structure having an octahedral sheet of uniform height (Mercier et al. 2005b).

The above conclusion differs from various views expressed in previous works (Lin and Guggenheim 1983; Weiss et al. 1985). We are the first to show that spatial constraints inherent to a geometric meso-octahedral sheet of uniform height impose the observed relationship (Eq. 6; Fig. 4) between the flattening angles of M1 and M2 sites and to argue that neither the average magnitude of the flattening angle nor the individual M1 and M2 flattening angle magnitudes are related to such geometric constraints. We show that differently sized M1 and M2 sites are accommodated by purely intra-octahedral-sheet geometric matching constraints (Eq. 6; Fig. 4), thereby removing the need to appeal to other mechanisms to explain M1 and M2 flattening-angle relationships. This implies that the flattening angle magnitudes themselves (and the average degree of flattening) are geometrically independent of the M1/M2 relationship (Eq. 6) and any associated degree of chemical ordering causing M1 and M2 size differences.

Tetrahedral-octahedral sheet matching

Next, consider the evidence that tetrahedral-octahedral sheet matching might affect octahedral flattening. Figure 6d shows that in the [Ann-Phl] and oxy-Bt single-crystal samples, which all have a near-$^{[IV]}(AlSi_3)$ tetrahedral composition, the flattening

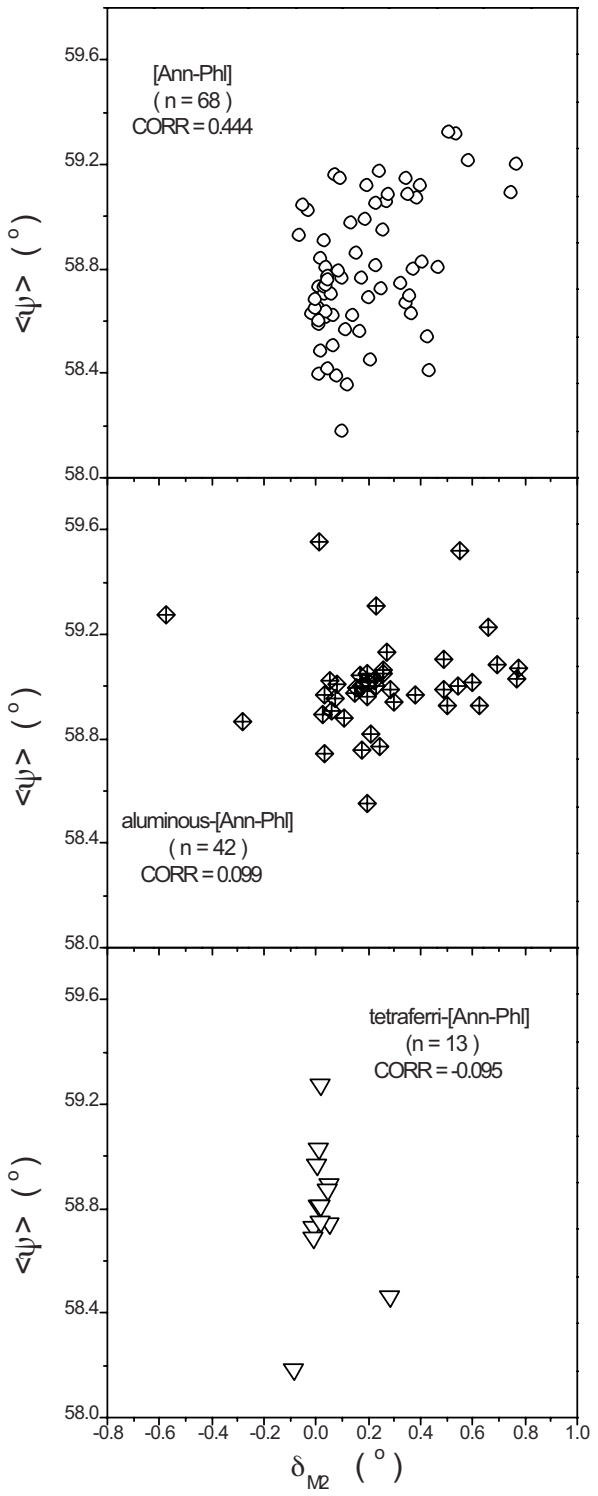

FIGURE 5. Plots of <ψ> vs. δ_{M2} (Table 3) for the various groups of single-crystal biotite-1*M* samples.

angle ψ_{M2} monotonously decreases as the average bond length <M2-O> increases. Such a correlation, although weaker, is also observed in the M1 sites of these [Ann-Phl] and oxy-Bt single-crystal samples (Fig. 6b). That the linear correlation observed is higher for M2 rather than M1 may be due to the greater number of M2 sites in the octahedral sheet (M2:M1 = 2:1), which allows its behavior to dominate whereas the M1 site simply adjusts; or it may be due to chemical order where more steric-effect active cations occupy the M1 sites (see below) and smaller more spherical cations (e.g., Al^{3+}, Fe^{3+}) occupy the M2 sites.

In addition to the M1/M2 difference in flattening behavior, it is important to note (Figs. 2, 3b, 6) that ψ *decreases* with increasing <M-O> values or octahedral cation size. This means that octahedral flattening decreases lateral expansion of the octahedral sheet relative to the expansion that would be related to increasing the octahedral cation bond length alone. This suggests that octahedral lateral expansion is resisted by the tetrahedral sheet, that is, that the tetrahedral sheet resists a *decrease* in α. The latter interpretation is not correct. An analysis of the bonding energetics (next section) shows that the observed behavior of ψ (Figs. 2, 3b, and 6) is predominantly the result of octahedral cation stereo-chemical bonding properties rather than octahedral-tetrahedral inter-sheet interactions.

Energetic constraints in ψ determination

Possibly the simplest realistic and predictive physical model of ψ that one can construct is one where the values of ψ are determined by the energetic compromises between (and combined actions of) three principle factors: (1) a preference of a given octahedral cation species for a particular local octahedral flattening, by virtue of its stereo-chemical bonding properties; (2) long-range ion-charge electrostatic effects, for example, where octahedral cation repulsion would favor increased flattening by moving the cations further away from each other and by screening the cations with oxygen anions between them; and (3) resistance or encouragement from the tetrahedral sheets, arising from an energetically preferred tetrahedral rotation angle for a given tetrahedral cation composition (e.g., Peterson et al. 1979). In general, bond lengths are determined with high cation-anion specificity whereas cation-anion-cation bond angles generally adjust to overall connectivity constraints. Thus, we expect that the first factor plays a more important role than the third because local cation-oxygen bonding constraints are expected to be stronger than cation-oxygen-cation bond-bending constraints.

We tested these ideas by constructing a mathematical model of the above energetics of ψ determination, in which we ignored the electrostatic term. This model assumes that bond stretching is energetically prohibitive and takes the free energy per unit of the T-O-T layer, U, to consist of three terms: a constant, C, that is ψ and α independent, a term linear in α, and a term linear in ψ. This is equivalent to a Tailor series expansion of U(α,ψ) to first order in the two variables, around a point close to observed values of α and ψ:

$$U(\alpha,\psi) = C + E_{tet}\,\alpha + E_{oct}\,\psi \qquad (7)$$

where E_{tet} and E_{oct} are physical constants having units of energy per radian. Given our assumption of no bond stretching, the octahedral and tetrahedral sheets must be commensurate, such that one has the added α-ψ constraint (obtained by equating Eqs. 1 and 3):

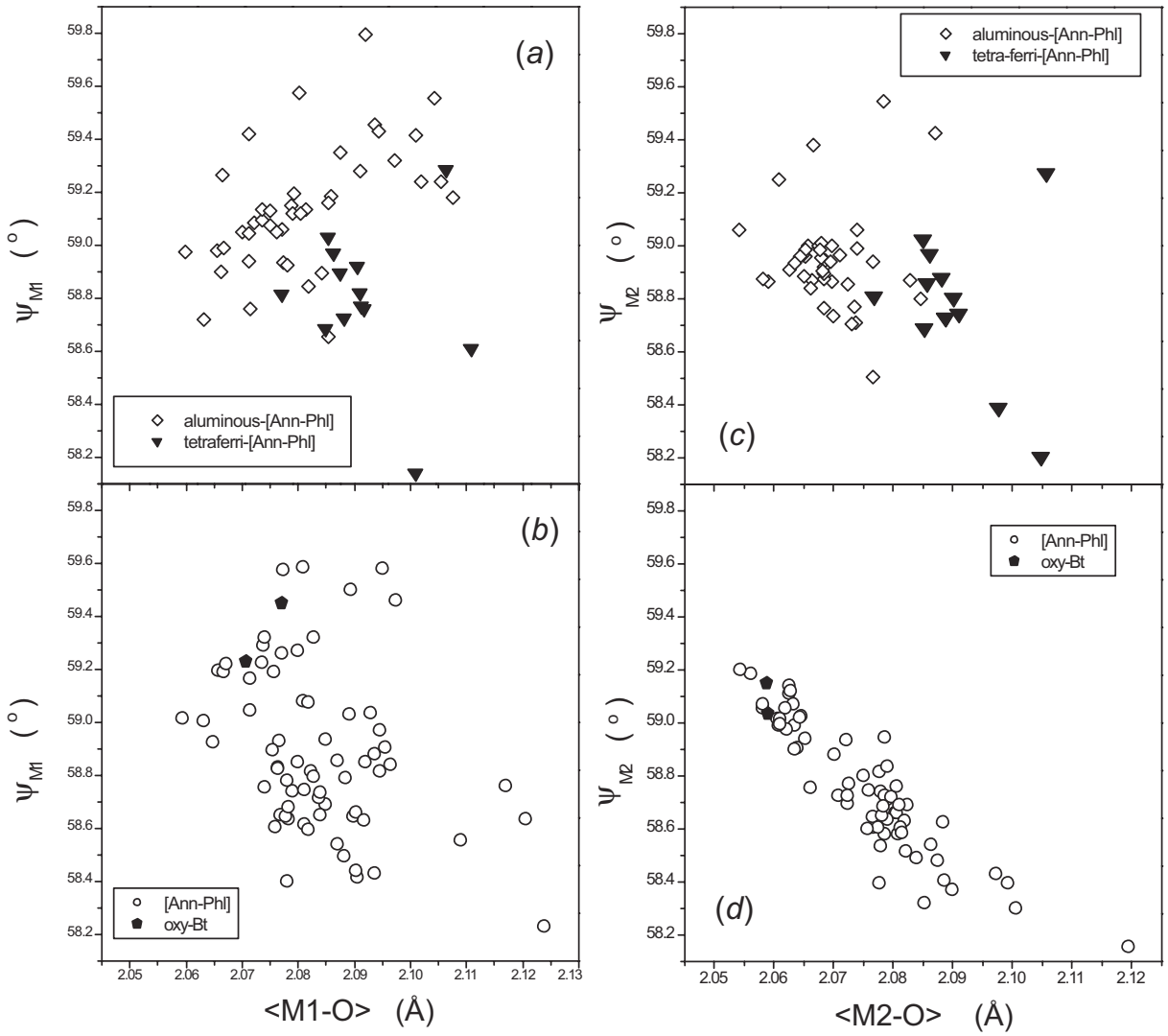

FIGURE 6. Flattening angle ψ_{M1} vs. <M1-O> (**a**, **b**) and ψ_{M2} vs. <M2-O> (**c**, **d**) for the various groups of single-crystal biotite-1*M* samples (Table 3).

$$\cos(\alpha) = [3\, d_o \sin(\psi)] / [4\, d_t^{bas} \sin(\tau_{bas} / 2)] \quad (8)$$

Therefore, Equation 7 is cast into a function of a single variable, either α or ψ. Values of α (or ψ) that minimize the energy, for given bond lengths and tetrahedral basal flattening (specific O_{bas}-T-O_{bas} tetrahedral basal bond angles, τ_{bas}, are preferred for a given tetrahedral sheet composition; see below), depend only on the dimensionless ratio E_{tet}/E_{oct} and only occur for positive values of this ratio. Because an increase in ψ away from the ideal value of ~54.74° corresponds to a more distorted octahedron and an increase in α away from 0° corresponds to a more distorted tetrahedral sheet, we expect both E_{tet} and E_{oct} to be positive. Indeed, we only find solutions consistent with the observed data (Fig. 6 and associated changes in α) for positive values. Also, to obtain observed values of α (<12°), E_{tet}/E_{oct} must be < 0.35. This is consistent with the idea that a change in tetrahedral rotation is easier to accomplish than a change in octahedral flattening. We conclude that $E_{oct}\psi$ is the dominant term in determining octahedral flattening and that it probably arises from the steric nature of the octahedral cation-oxygen bond. This, in turn, implies that E_{oct} depends on the octahedral cation species. The simplest way to model the latter "compositional" dependence is to assume a linear dependence of E_{oct} on d_o as:

$$E_{oct} = \delta_0 + \delta_1\, d_o \quad (9)$$

Because ψ decreases with d_o (Fig. 6), δ_1 must be positive and sufficiently large to produce the observed effect.

This simple model reproduces observed variations in α and ψ with d_o for the main Mg-Fe mica solid solutions. If it is correct, it implies that the decrease in ψ with increasing <M-O> is related to octahedral cation stereo-chemical bonding properties and that tetrahedral-octahedral inter-sheet interactions cannot contribute to this decrease because the sign of E_{tet} is the opposite of what it would need to be to amplify the effect. In other words, the local steric requirements on ψ are sufficiently strong to overcome

the weaker countering influence of the tetrahedral sheets and the variations in ψ with d_o are smaller than they would be for an isolated octahedral sheet.

The latter conclusion and the related conclusions that octahedral cation stereo-chemical bonding properties predominantly determine ψ and that a change in tetrahedral rotation is easier to accomplish than a change in octahedral flattening all go against the idea that in biotite, octahedral flattening is a mechanism for alleviating tetrahedral-octahedral sheet mismatch. Instead, octahedral flattening increases the sheet mismatch energy, in that it increases the tetrahedral sheet energy. One should consider that octahedral flattening is predominantly determined by octahedral cation composition, as is the mean octahedral cation bond length, and that the resulting lateral dimensions of the octahedral sheet must consequently be accommodated by adjustments in the tetrahedral sheets, predominantly via tetrahedral rotation for a given tetrahedral cation composition and associated tetrahedral basal flattening angle.

TETRAHEDRAL FLATTENING AND TETRAHEDRAL ROTATION LIMITS

Composition-specific tetrahedral basal flattening

Tetrahedral flattening occurs and is important to include in any quantitative crystal chemical analysis of the tetrahedral sheet, if a quantitative analysis of tetrahedral rotation is required. Figures 7 and 8 display the average basal tetrahedral edge length $<O_{bas}\text{-}O_{bas}>$ as a function of the average basal tetrahedral bond length $<T\text{-}O_{bas}>$ (Table 3) for the 175 single-crystal 1*M* samples and for the single-crystal biotite-1*M* samples, respectively. The lines in these figures correspond to tetrahedral flattening $O_{bas}\text{-}T\text{-}O_{bas}$ angle τ_{bas} = constant predictions made using the following relationship (Mercier et al. 2005a; Eq. B-7a, Fig. B-2, Appendix B):

$$e_t^{bas} = 2\, d_t^{bas} \sin(\tau_{bas}/2) \quad (10)$$

where e_t^{bas} is the length of the three $O_{bas}\text{-}O_{bas}$ basal edges, d_t^{bas} is the length of the three $T\text{-}O_{bas}$ bonds, and τ_{bas} is the value of the three $O_{bas}\text{-}T\text{-}O_{bas}$ angles. Figure 7 shows that the K-rich samples display fair agreement with the τ_{bas} = 108.5° prediction (solid line), whereas other groups of samples having different tetrahedral sheet and/or interlayer contents occur at other values of τ_{bas} (cf. Brigatti and Guggenheim 2002). In the case of the biotite-1*M* samples (Fig. 8), most of the aluminous-[Ann-Phl] and tetraferri-[Ann-Phl] samples lie above the τ_{bas} = 108.5° prediction line, whereas the [Ann-Phl] and oxy-Bt samples closely follow the latter prediction line.

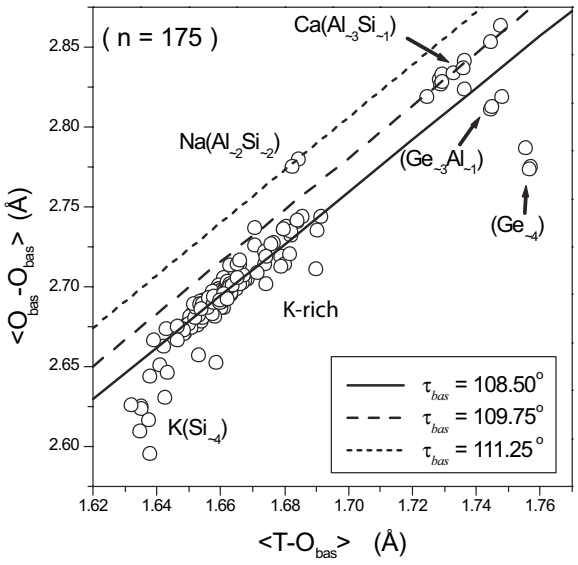

FIGURE 7. Average basal tetrahedral edge length $<O_{bas}\text{-}O_{bas}>$ vs. the average basal tetrahedral bond length $<T\text{-}O_{bas}>$ (Table 3) for the 175 single-crystal 1*M* refinements. The various lines correspond to predictions (validated in Appendix B) that are explained in the text.

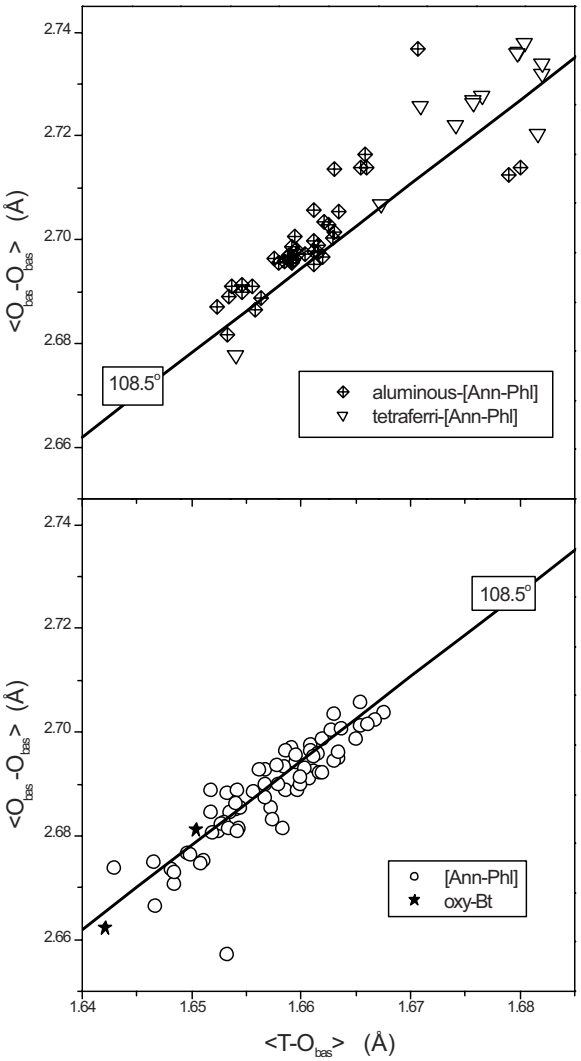

FIGURE 8. Average basal tetrahedral edge length $<O_{bas}\text{-}O_{bas}>$ vs. the average basal tetrahedral bond length $<T\text{-}O_{bas}>$ (Table 3) for the various groups of single-crystal biotite-1*M* samples.

Upper limit of the tetrahedral rotation angle

Figure 9 shows the calculated tetrahedral rotation angle, α_{calc}, as a function of the octahedral-to-tetrahedral cation-anion bond length ratio, $\langle M\text{-}O\rangle_{calc}/\langle T\text{-}O_{bas}\rangle_{calc}$, for various solid solution series of synthetic powder samples. $\langle T\text{-}O_{bas}\rangle_{calc}$ is the mean basal tetrahedral bond length calculated in the same manner as for $\langle M\text{-}O\rangle_{calc}$ via Equation 4b. For a given synthetic powder sample, α_{calc} is obtained from the measured *b* and calculated $\langle T\text{-}O_{bas}\rangle_{calc}$ values via Equation 2b assuming that $\tau_{bas} = 108.5°$ (Figs. 7 and 8). The various predictions that are displayed as thin solid lines in Figure 9 are obtained using Equations 1b and 3b at a given octahedral flattening angle ψ with $\tau_{bas} = 108.5°$ (Figs. 7 and 8).

For a given value of tetrahedral flattening τ_{bas}, the point of initiation of the lower limit of $\alpha = 0°$ (illustrated by the positions of the small arrows shown in Fig. 9) moves from lower to higher $\langle M\text{-}O\rangle_{calc}/\langle T\text{-}O_{bas}\rangle_{calc}$ ratio as the octahedral flattening ψ increases. The lower limit of $\alpha = 0°$ corresponds to the point where fully extended tetrahedral sheets cannot laterally fit onto larger octahedral sheets. On the basis of the structural parameters that were taken to occur for octahedra ($\langle M\text{-}O\rangle_{calc}$, ψ) and tetrahedra ($\langle T\text{-}O_{bas}\rangle_{calc}$, τ_{bas}), note that all the annite (Fe end-member) synthetic powder samples fall in a regime where octahedral and tetrahedral sheets cannot be matched, as predicted by Hazen and Wones (1972).

The upper limit of α shown in Figure 9 for the Mg-Ni JLR series, which corresponds to the break in *b* seen in Figure 1, occurs regardless of any set of cation-specific basal tetrahedral bond lengths $d_t^{bas}(T_i)$ taken between Shannon values and the ones used in this paper (Table 4). The only difference is that slightly different plateau values for α are obtained. Here, with the structural parameters that are assumed, an upper limit of $\alpha \leq 9.5°$ is obtained. The same upper limit is also obtained in the Ann-oxy-ferrioxy series (Fig. 9), where all samples have a tetrahedral composition of $^{[IV]}(Al_{0.88}Si_3Fe^{3+}_{0.12})$ (Rancourt et al. 1994a, 2001). Note that the particular upper limit value of $\alpha = 9.5°$ is corroborated, as shown below (Figs. 10–12), by a detailed examination of available structural refinement data, thereby lending further support to the characteristic cation- and coordination-specific bond length values used in this work (Table 4, Appendix C).

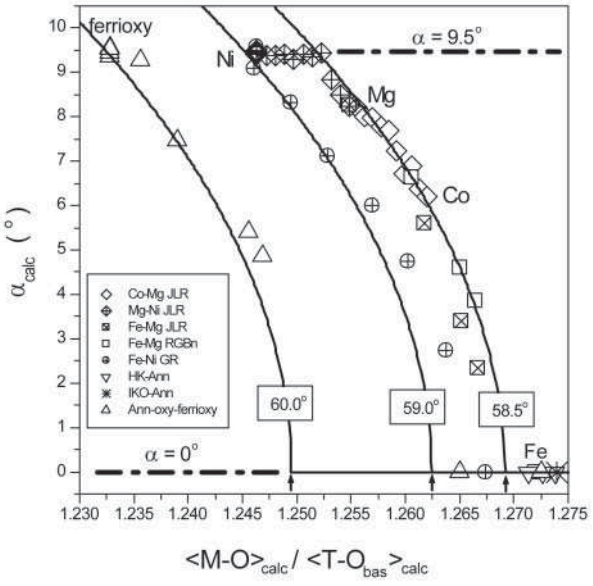

FIGURE 9. Calculated tetrahedral rotation angle α_{calc} as a function of the octahedral-to-tetrahedral cation-anion bond length ratio $\langle M\text{-}O\rangle_{calc}/\langle T\text{-}O_{bas}\rangle_{calc}$ (Eq. 4) for the synthetic powder samples.

Figures 10a–c show the average tetrahedral rotation angle α as a function of the bond length ratio $\langle M\text{-}O\rangle/\langle T\text{-}O\rangle_{bas}$ (Table 3) for the 175 single-crystal 1*M* samples and for the single-crystal biotite-1*M* samples, respectively. The dashed-dotted horizontal lines displayed in these figures are drawn at the same α positions as those illustrated in Figure 9. Note that Figure 10a is shown on an overall scale, while Figure 10b has the same horizontal and vertical scales as Figure 9. In examining Figures 10b and 10c, note that the density of the data points is higher near the dashed-dotted line positioned at $\alpha = 9.5°$. Redhammer and Roth (2002) made similar observations by plotting the average tetrahedral rotation angle α as a function of the mean octahedral cation radii, calculated using the tables of Shannon (1976), for a subset of the 175 single-crystal 1*M* samples considered here.

Figure 11 presents the distribution of α for all 175 single-crystal 1*M* structures. The distribution is clearly asymmetric. All samples outside the main trend displayed by the biotite-1*M* samples belong to groups that have significantly different tetrahedral-sheet contents, except for the paragonite dioctahedral mica [ideally $Na(Al_2\square)(AlSi_3)O_{10}(OH)_2$] refined by Soboleva et al. (1977). In the same connexion, Figure 12 shows the distributions of α for the [Ann-Phl], aluminous-[Ann-Phl], and tetraferri-[Ann-Phl] groups separately. Overall, Figure 12 represents further evidence that an upper limit is present at $\alpha \cong 9.5°$ for the [Ann-Phl] samples, although it is less compelling than the observed break in *b* in the synthetic Mg-Ni series (Fig. 1) and the associated analysis (Fig. 9). Moreover, as discussed by Hazen and Wones (1978), Figure 12 suggests that an upper limit on α is tetrahedral composition dependent.

Comparison with the lower limit and impact on octahedral flattening

The lower limit on α ($\alpha = 0°$) corresponds to a fully extended tetrahedral sheet in its maximum lateral extension state. Beyond this point, bond breakage by over stretching or intra-tetrahedral oxygen-cation-oxygen bond angle bending away from the preferred tetrahedral composition-specific τ_{bas} angle (Figs. 7 and 8) must occur if a larger tetrahedral sheet is imposed. In contrast, the upper limit on α does not arise from such stringent conditions because, from a geometric perspective, a smaller octahedral sheet could simply be accommodated by more tetrahedral rotation (i.e., a larger value of α) without any geometrically required bond stretching or bending.

The lower limit on α ($\alpha = 0°$) is intrinsically a tetrahedral sheet property and causes necessary adjustments in octahedral sheets that would otherwise be too large, such as the well-known oxidation and cation-exchange mechanisms in annite (Hazen and Wones 1972; Redhammer et al. 1993; Mercier et al. 1996, 1999; Rancourt et al. 1994a, 2001). On the other hand, one could argue

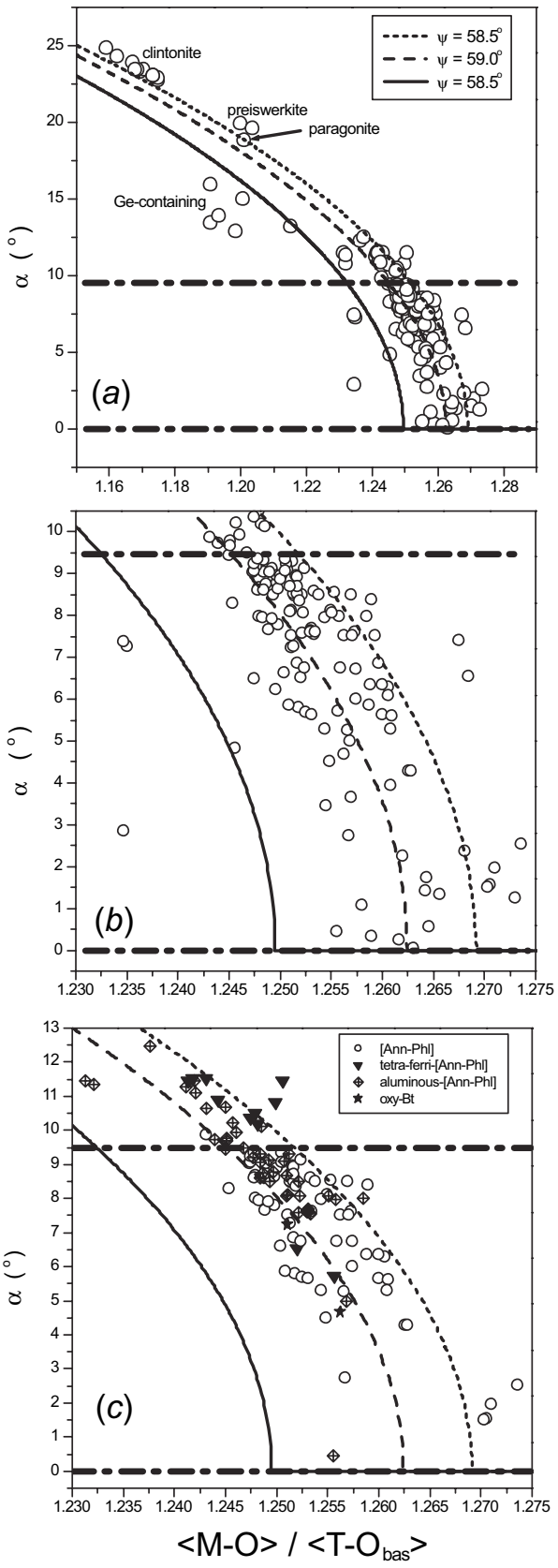

◀ **FIGURE 10.** Average tetrahedral rotation angle α vs. the ratio <M-O>/<T-O_{bas}> (Table 3) observed for: the 175 single-crystal 1*M* refinements (**a**) = overall scale, (**b**) = same horizontal and vertical scales as Figure 9; and (**c**) the various groups of single-crystal biotite-1*M* samples. The dashed-dotted lines that are displayed are drawn at the same α positions as those illustrated in Figure 9.

that the observed upper limit on α is caused by the octahedral sheet that, for example, in the Mg-Ni series (Fig. 1) would have an average octahedral flattening angle that would vary in the right way to cause a constant octahedral (and tetrahedral) lateral extension. This seems unlikely compared to the simpler explanation, for example, that bond bending of cation-oxygen-cation bridging bonds between neighboring tetrahedra in the tetrahedral sheet is energetically prohibitive beyond some effectively critical value. The simpler interpretation where the upper limit on α, like the lower limit, is also intrinsically a tetrahedral sheet property, explains as well why the ferrioxyannite samples show the same value of the upper limit α (Fig. 9) and why changing the composition of the tetrahedral sites alone (for a given interlayer cation composition) appears to change the value of the upper limit α (and the tetrahedral composition-specific value of the tetrahedral basal flattening angle) (Figs. 7, 8, 9, and 12). We conclude that the observed upper limit on α is primarily a tetrahedral sheet property and that it imposes the observed concomitant octahedral flattening adjustments.

Possible cause of the upper limit in tetrahedral rotation

The only previous attempt to explain a possible upper limit on α observed in both synthetic powders (Fig. 9) and natural biotite-1*M* single crystals (Fig. 12) was that of Hewitt and Wones (1975). They suggested that *interlayer* bonding constraints may give rise to a maximum tetrahedral rotation. They also suggested

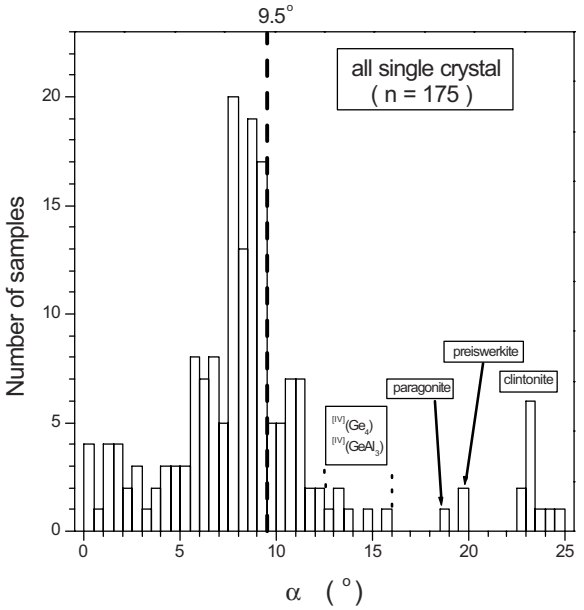

FIGURE 11. Distribution of α (Table 3) for the 175 single-crystal 1*M* refinements. The dashed line corresponds to α = 9.5°.

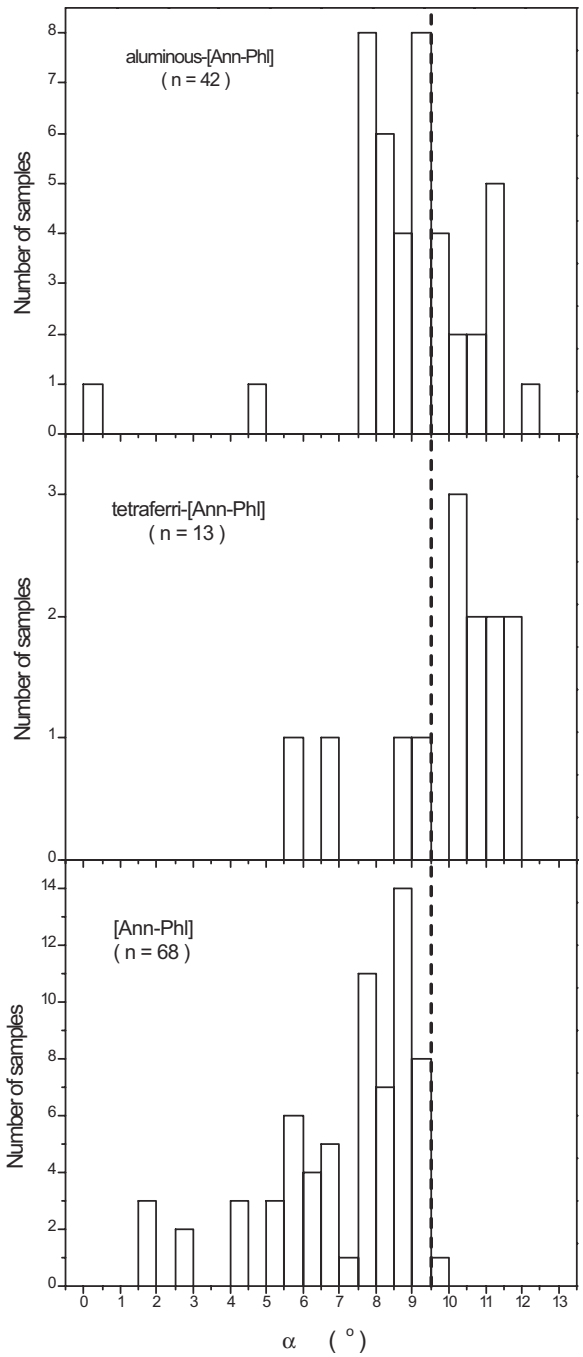

FIGURE 12. Distribution of α (Table 3) for various groups of single-crystal biotite-1*M* samples. The dashed lines correspond to α = 9.5°.

that an upper limit on α was the reason that Al-substitutions in synthetic biotite solid solutions cease at a tetrahedral-octahedral composition of $^{[IV]}(Al_{1.75}Si_{2.25})$-$^{[VI]}([Fe,Mg]_{2.25}Al_{0.75})$.

The argument of Hewitt and Wones (1975) was based on calculated α-rotation angles and interlayer K-O bond lengths obtained using Figure 4 of Donnay et al. (1964b), who assumed regular tetrahedra in their calculations. The α-rotation and K-O bond lengths that Hewitt and Wones (1975) obtained from the lattice parameters of their most aluminous synthetic biotites ranged from 12° and 2.89 Å in their Mg-free samples to 14° and 2.77 Å in their Fe-free samples. The accepted range of bond lengths for K with coordinations between 6 and 12 range from 2.76 to 3.16 Å (e.g., Shannon 1976) and led Hewitt and Wones to propose that the interlayer site controls the maximum value of α and thus the maximum amount of Al substitution, because Al substitution in biotite via the Tschermak's substitution [i.e., $^{[VI]}(Fe^{2+}, Mg^{2+}) + {}^{[IV]}Si^{4+} \leftrightarrow {}^{[VI]}Al^{3+} + {}^{[IV]}Al^{3+}$] increases the amount of necessary tetrahedral rotation α, that in turn directly impacts the interlayer cation environment.

However, the tetrahedra of actual 1*M* micas are not regular (Figs. 7 and 8; Fig. B-2, Appendix B; Brigatti and Guggenheim 2002) and this strongly affects calculated α-rotation and interlayer bond lengths (e.g., Takeda and Morosin 1975). Moreover, the inner (i.e., first nearest neighbor) interlayer site bond lengths actually observed in single-crystal K-rich 1*M* polytype *C*2/*m* space group micas ranges from ~2.90 to ~3.15 Å (e.g., Brigatti and Guggenheim 2002; Mercier 2003). Using the reasoning of Hewitt and Wones (1975), we found that the interlayer K-O bond lengths actually observed in real mica samples are not a limiting factor for α.

We therefore reaffirm our conclusion that the upper limit of α ≤ 9.5° present in K-rich 1*M* micas having a near-$^{[IV]}(AlSi_3)$ tetrahedral composition, for both synthetic powders and natural single crystals, is predominantly determined by the tetrahedral sheets themselves. We attribute the latter upper limit on α to a tetrahedral-sheet bond bending limit. Further work to quantify upper limit α values for other tetrahedral sheet compositions (as suggested by Fig. 12) and to attempt electronic structure calculations that would elucidate the physical cause of a maximum value of α, in terms of electronic distributions and energies, would be of great interest.

IMPLICATIONS FOR THE STABILITY RELATIONSHIPS OF MICAS

Structural limits (that can be expressed as geometrical limits) must have implications for thermodynamic stability because such limits are fundamentally caused by energy (bonding energy) constraints. The next question is the *extent* to which a particular structural constraint will affect stability relations (on a *P-T* diagram) and compositional limits. A quantitative answer to this question for our observed upper tetrahedral rotation limit is beyond the scope of the present paper, however one can qualitatively ascertain how this limit might act. In particular, we can do this in comparison to some of the known effects of the lower tetrahedral rotation (α = 0) limit.

That the maximum lateral extension (α = 0°) limit significantly affects the energetics of annite, to the point of disallowing the ideal end-member composition, is well established (e.g., Rancourt et al. 2001) and shows that the tetrahedral sheet can impose a strict stability limit rather than always simply adapting (by tetrahedral rotation) to the octahedral sheet. Similarly, if the tetrahedral sheet also imposes a minimum lateral extension ($\alpha = \alpha_{max}$) limit, then this must also restrict the octahedral sheet at the small lateral extension end in a way that will increase the octahedral sheet free energy compared to not being subjected to this limit.

It has been argued that such an $\alpha = \alpha_{max}$ limit is responsible for the observed substitution limit on the total Al content of synthetic Al-rich biotites (Hewitt and Wones 1975). We found that a sharp $\alpha = \alpha_{max}$ limit occurs, but that it is tetrahedral composition dependent. We found $\alpha_{max} = 9.5°$ for $^{IV}(AlSi_3)$ and observed that this limit is strictly obeyed for all K-rich near-$AlSi_3$ tetrahedral composition samples studied (both natural and synthetic). That this limit occurs in natural samples from rocks might be taken to imply that strict compositional limits are imposed on the mica phase and that element partitioning is constrained by this geometric limit in mica. The latter is only true, however, if the octahedral sheet cannot accommodate the lateral extension limit by changing the octahedral flattening ψ, for example. We must therefore examine the energetics of octahedral flattening in establishing whether or not tetrahedral rotational limits will significantly affect composition and stability.

We have argued that changes in octahedral flattening are more energetically prohibitive than tetrahedral rotation, but is octahedral flattening resistance strong enough to significantly affect mineral stability? Clearly, at the maximum extension (annite) end the octahedral *straightening* that would be required is energetically prohibited and chemical composition adjustments are imposed. At the minimum extension ($\alpha = \alpha_{max}$) end, *extra* flattening is required if smaller octahedral cations are to be accommodated. Our measurements of the synthetic Mg-Ni series show an example where such extra flattening does occur, leading to a constant *b* despite increased Ni. Therefore, extra octahedral flattening imposed by a lower limit in tetrahedral extension need not be energetically prohibited. On the other hand, we argue that the resistance to changes in octahedral flattening is a steric property that depends on the octahedral cation identity. Therefore, resistance to increased octahedral flattening at the $\alpha = \alpha_{max}$ limit could vary significantly with octahedral cation species and could be important in determining stability limits in natural systems.

ACKNOWLEDGMENTS

We thank R.J. Evans for helpful discussions. We thank S. Guggenheim for critical comments to the manuscript. Financial support from the Natural Sciences and Engineering Research Council of Canada in the form of a Discoveries Grant to D.G.R. is gratefully acknowledged. P.H.J.M. acknowledges financial support from Ontario Graduate Scholarships in Science and Technology in association with Golder Associates and Noranda.

REFERENCES CITED

Alietti, E., Brigatti, M.F., and Poppi, L. (1995) The crystal structure and chemistry of high-aluminum phlogopite. Mineralogical Magazine, 59, 149–157.

——— (1997) Clintonite-1*M*: Crystal chemistry and its relationships to closely associated Al-rich phlogopite. American Mineralogist, 82, 936–945.

Bailey, S.W., (Ed.) (1984a) Micas, vol. 13, 584 pp. Reviews in Mineralogy and Geochemistry, Mineralogical Society of America, Chantilly, Virginia.

——— (1984b) Crystal chemistry of the true micas. In S.W. Bailey, Ed., Micas, 13, 13–60. Reviews in Mineralogy and Geochemistry, Mineralogical Society of America, Chantilly, Virginia.

——— (Ed.) (1988) Hydrous phyllosilicates (exclusive of micas), vol. 19, 725 pp. Reviews in Mineralogy and Geochemistry, Mineralogical Society of America, Chantilly, Virginia.

Birle, J.D., Gibbs, G.V., Moore, P.B., and Smith, J.V. (1968) Crystal structures of natural olivines. Ammerican Mineralogist, 53, 807–824.

Böstrom, D. (1987) Single-crystal X-ray diffraction studies of synthetic N-Mg olivine solid solutions. American Mineralogist, 72, 965–972.

Brigatti, M.F. and Davoli, P. (1990) Crystal-structure refinements of 1*M* plutonic biotites. American Mineralogist, 75, 305–313.

Brigatti, M.F. and Guggenheim, S. (2002) Mica crystal chemistry and the influence of pressure, temperature, and solid solution on atomistic models. In A. Mottana, F.P. Sassi, J.B. Thompson, and S. Guggenheim, Eds., Micas. Reviews in Mineralogy and Geochemistry, 46, 1–97. Mineralogical Society of America and the Geochemical Society, Washington, D.C.

Brigatti, M.F. and Poppi, L. (1993) Crystal chemistry of Ba-rich trioctahedral micas-1*M*. European Journal of Mineralogy, 5, 857–871.

Brigatti, M.F., Galli, E., and Poppi, L. (1991) Effect of Ti substitution on biotite-1*M* crystal chemistry. American Mineralogist, 76, 1174–1183.

Brigatti, M.F., Medici, L., and Poppi, L. (1996a) Refinement of the structure of natural ferriphlogopite. Clays and Clay Minerals, 44, 540–545.

Brigatti, M.F., Medici, L., Saccani, E., and Vaccaro, C. (1996b) Crystal chemistry and petrologic significance of Fe^{3+}-rich phlogopite from the Tapira carbonatite complex, Brazil. American Mineralogist, 81, 913–927.

Brigatti, M.F., Frigieri, P., Ghezzo, C., and Poppi, L. (2000a) Crystal chemistry of Al-rich biotites coexisting with muscovites in peraluminous granites. American Mineralogist, 85, 436–448.

Brigatti, M.F., Lugli, C., Poppi, L., Foord, E.E., and Kile, D.E. (2000b) Crystal chemical variations in Li- and Fe-rich micas from Pikes Peak batholith (central Colorado). American Mineralogist, 85, 1275–1286.

Brigatti, M.F., Medici, L., Poppi, L., and Vaccaro, C. (2001) Crystal chemistry of trioctahedral-1*M* micas from the Alto Paranaíba igneous province, southeastern Brazil. Canadian Mineralogist, 39, 1333–1345.

Brigatti, M.F., Guggenheim, S., and Poppi, M. (2003a) Crystal chemistry of the 1*M* mica polytype: The octahedral sheet. American Mineralogist, 88, 667–675.

Brigatti, M.F., Caprilli, E., Marchesini, M., and Poppi, L. (2003b) The crystal structure of roscoelite-1*M*. Clays and Clay Minerals, 51, 301–308.

Brown, I.D. and Altermatt, D. (1985) Bond-valence parameters obtained from a systematic analysis of the inorganic crystal structure database. Acta Crystallographica, B41, 244–247.

Cruciani, G. and Zanazzi, P.F. (1994) Cation partitioning and substitution mechanisms in 1*M* phlogopite: A crystal chemical study. American Mineralogist, 79, 289–301.

Donnay, G., Donnay, J.D.H., and Takeda, H. (1964a) Trioctahedral one-layer micas. II. Prediction of the structure from composition and cell dimensions. Acta Crystallographica, 17, 1374–1381.

Donnay, G., Morimoto, N., Takeda, H., and Donnay, J.D.H. (1964b) Trioctahedral one-layer micas. I. Crystal structure of a synthetic iron mica. Acta Crystallographica, 17, 1369–1373.

Ďurovič, S. (1994) Classification of phillosilicates according to the symmetry of their octahedral sheets. Ceramics-Silikáty, 38, 81–84.

Eggleton, R.A. and Ashley, P.M. (1989) Norrshite, a new manganese mica, $K(Mn^{3+}_2Li)Si_4O_{12}$, from the Hoskins mine, New South Wales, Australia. American Mineralogist, 74, 1360–1367.

Ferraris, G. and Ivaldi, G. (2002) Structural Features of Micas. In A. Mottana, F.P. Sassi, J.B. Thompson, and S. Guggenheim, Eds., Micas, vol. 46, 117–153. Reviews in Mineralogy and Geochemistry, Mineralogical Society of America, Chantilly, Virginia.

Gibbs, G.V., Tamada, O., and Boisen Jr., M.B. (1997) Atomic and ionic radii: a comparison with radii derived from electron density distributions. Physics and Chemistry of Minerals, 24, 432–439.

Guggenheim, S. (1984) The brittle micas. In S.W. Bailey, Ed., Micas. Reviews in Mineralogy and Geochemistry, 13, 61–104. Mineralogical Society of America and the Geochemical Society, Washington, D.C.

Guggenheim, S., Chang, Y.-H., and Koster van Groos, A.F. (1987) Muscovite dehydroxylation: High-temperature studies. American Mineralogist, 72, 537–550.

Hazen, R.M. (1976) Effects of temperature and pressure on the crystal structure of forsterite. American Mineralogist, 61, 1280–1293.

——— (1977) Effects of temperature and pressure on the crystal structure of ferromagnesian olivine. American Mineralogist, 62, 286–295.

Hazen, R.M. and Burnham, C.W. (1973) The crystal structures of one-layer phlogopite and annite. American Mineralogist, 58, 889–900.

Hazen, R.M. and Wones, D.R. (1972) The effect of cation substitutions on the physical properties of trioctahedral micas. American Mineralogist, 57, 103–129.

——— (1978) Predicted and observed compositional limits of trioctahedral micas. American Mineralogist, 63, 885–892.

Hewitt, D.A. and Wones, D.R. (1975) Physical properties of some synthetic Fe-Mg-Al trioctahedral biotites. American Mineralogist, 60, 854–862.

Lager, G.A. and Meagher, E.P. (1978) High-temperature structural study of six olivines. American Mineralogist, 63, 365–377.

Lalonde, A.E., Rancourt, D.G., and Ping, J.Y. (1998) Accuracy of ferric/ferrous determinations in micas: A comparison of Mössbauer spectroscopy and the Pratt and Wilson wet-chemical methods. Hyperfine Interactions, 117, 175–204.

Lin, J.-C., and Guggenheim, S. (1983) The crystal structure of Li, Be-rich brittle mica: a dioctahedral-trioctahedral intermediate. American Mineralogist, 68, 130–142.

Mercier, P.H.J. (2003) Crystal Chemistry of Natural and Synthetic Trioctahedral Micas: Exploring the Limits of Geometric Crystal Chemical Models. Ph.D. Thesis, 253 pp. University of Ottawa, Ottawa, Ontario, Canada.

Mercier, P.H.J., Rancourt, D.G., and Berman, R.G. (1996) Aspects of the crystal

chemistry of annite mica. In I. Ortalli, Ed., Conference Proceedings, International Conference on the Application of the Mössbauer Effect, ICAME-1995, Volume 50, 789–792. Italian Physical Society.
Mercier, P.H.J., Rancourt, D.G., Berman, R.G., and Robert, J.-L. (1999) Control of site population, at synthesis, by inter-sheet thermal expansion in a 2:1 layer silicate. In H. Hodama, A.R. Mermut, and J.K. Torrance, Eds., Clays for our future, 221–227. Proceedings of the 11th International Clay Conference, Ottawa, Canada.
Mercier, P.H.J., Evans, R.J., and Rancourt, D.G. (2005a) Geometric crystal chemical models for structural analysis of micas and their stacking polytypes. American Mineralogist, 90, 382–398.
Mercier, P.H.J., Rancourt, D.G., Robert, J.-L., Berman, R.G., and Redhammer, G.J. (2005b) Fundamental difference between synthetic powder and natural or synthetic single crystal 1*M* micas: Geometric homo-octahedral versus geometric meso-octahedral sheets. American Mineralogist, 90, 399–410.
Morimoto, N., Tokonami, M., Watanabe, M., and Koto, K. (1974) Crystal structures of three polymorphs of Co_2SiO_4. American Mineralogist, 59, 475–485.
Myake, M., Nakamura, H., Kojima, H., and Marumo, F. (1987) Cation ordering in Co-Mg olivine solid-solution series. American Mineralogist, 72, 594–598.
Nespolo, M. and Ďurovič, S. (2002) Crystallographic basis of polytypism and twinning in micas. In A. Mottana, F.P. Sassi, J.B. Thompson, and S. Guggenheim, Eds., Micas. Reviews in Mineralogy and Geochemistry, 46, 155–279. Mineralogical Society of America, Washington, D.C.
Nord, A.G., Annersten, H., and Filippidis, A. (1982) The cation distribution in synthetic Mg-Fe-Ni olivines. American Mineralogist, 67, 1206–1211.
Peterson, R.C., Hill, R.J., and Gibbs, G.V. (1979) A molecular-orbital study of distortions in the layer structures brucite, gibbsite and serpentine. Canadian Mineralogist, 17, 703–711.
Press, W.H., Teukolsky, S.A., Vetterling, W.T., and Flannery, B.P. (1992) Numerical recipes in Fortran: the art of scientific computing, 963 pp. Cambridge University Press, New York, U.S.A.
Rajamani, V., Brown, G.E., and Prewitt, C.T. (1975) Cation ordering in Ni-Mg olivine. American Mineralogist, 60, 292–299.
Rancourt, D.G. (1989) Accurate site populations from Mössbauer spectroscopy. Nuclear Instruments and Methods in Physics Research B (NIMB), 44, 199–210.
——— (1998) Mössbauer spectroscopy in clay science. Hyperfine Interactions, 117, 3–38.
Rancourt, D.G. and Ping, J.Y. (1991) Voigt-based methods for arbitrary-shape static hyperfine parameter distributions in Mössbauer spectroscopy. Nuclear Instruments and Methods in Physics Research B (NIMB), 58, 85–97.
Rancourt, D.G., McDonald, A.M., Lalonde, A.E., and Ping, J.Y. (1993) Mössbauer absorber thicknesses for accurate site populations in Fe-bearing minerals. American Mineralogist, 78, 1–7.
Rancourt, D.G., Christie, I.A.D., Royer, M., Kodama, H., Robert, J.-L., Lalonde, A.E., and Murad, E. (1994a) Determination of accurate $^{[4]}Fe^{3+}$, $^{[6]}Fe^{3+}$, and $^{[6]}Fe^{2+}$ site populations in synthetic annite by Mössbauer spectroscopy. American Mineralogist, 79, 51–62.
Rancourt, D.G., Ping, J.Y., and Berman, R.G. (1994b) Mössbauer spectroscopy of minerals. III. Octahedral-site Fe^{2+} quadrupole splitting distributions in the phlogopite-annite series. Physics and Chemistry of Minerals, 21, 258–267.
Rancourt, D.G., Mercier, P.H.J., Cherniak, D.J., Desgreniers, S., Hodama ,H., Robert, J.-L., and Murad, E. (2001) Mechanisms and crystal chemistry of oxidation in annite: Resolving the hydrogen-loss and vacancy reactions. Clays and Clay Minerals, 49, 455–491.
Redhammer, G.J. and Roth, G. (2002) Single-crystal structure refinements and crystal chemistry of synthetic trioctahedral micas $KM_3(Al^{3+},Si^{4+})_4O_{10}(OH)_2$, where M = Ni^{2+}, Mg^{2+}, Co^{2+}, Fe^{2+}, or Al^{3+}. American Mineralogist, 87, 1464–1476.
Redhammer, G.J., Beran, A., Dachs, E., and Amthauer, G. (1993) A Mössbauer and X-ray diffraction study of annites synthesized at different oxygen fugacities and crystal chemical implications. Physics and Chemistry of Minerals, 20, 382–394.
Royer, M. (1991) Site-specific Fe-57 Mössbauer recoilless fractions in true trioctahedral micas. M.Sc. Thesis, 111 pp. University of Ottawa, Ontario, Canada.
Russell, R.L. and Guggenheim, S. (1999) Crystal structures of hydroxyphlogopite at high temperatures and heat-treated biotites: The influence of the O,OH,F site. Canadian Mineralogist, 37, 711–720.
Shannon, R.D. (1976) Revised effective ionic radii and sytamatic studies of interatomic distances in halides and chalcogenides. Acta Crystallographica, A32, 751–767.
Smyth, J.R. (1975) High temperature crystal chemistry of fayalite. American Mineralogist, 60, 1092–1097.
Smyth, J.R. and Hazen, R.M. (1973) The crystal structures of forsterite and hortonolite at several temperatures up to 900 °C. American Mineralogist, 58, 588–593.
Soboleva, S.V., Sidorenko, O.V., and Zvyagin, B.B. (1977) Crystal structure of paragonite 1*M*. Soviet Physics Crystallography, 22, 291–293.
Takeda, H. and Morosin, B. (1975) Comparison of observed and predicted structural parameters of mica at high temperature. Acta Crystallographica, B31, 2444–2452.
Toraya, H. (1981) Distortions of octahedra and octahedral sheets in 1*M* micas and the relation to their stability. Zeitschrift für Kristallographica, 157, 173–190.
Tyrna, P.L. and Guggenheim, S. (1991) The crystal structure of norrishite, $KLiMn_2^{3+}Si_4O_{12}$: An oxygen-rich mica. American Mineralogist, 76, 266–271.
Weiss, Z., Rieder, M., Chmielovà, M., and Krajíček, J. (1985) Geometry of the octahedral coordination in micas: a review of refined structures. American Mineralogist, 70, 747–757.
Weiss, Z., Rieder, M., and Chmielovà, M. (1992) Deformation of coordination polyhedra and their sheets in phillosilicates. European Journal of Mineralogy, 4, 665–682.

Manuscript received September 15, 2004
Manuscript accepted September 13, 2005
Manuscript handled by Lee Groat

Appendix B. Validation of geometric crystal chemical models for octahedral and tetrahedral sheets

Octahedral sheet

By using parameters that characterize the octahedral sites, the in-plane *a* and *b* lattice parameters can be expressed as (Mercier et al. 2005a):

$$a = 3 \cdot d_o \cdot \sin\psi \quad \text{(B-1a)}$$
$$b = 3 \cdot 3^{1/2} \cdot d_o \cdot \sin\psi \quad \text{(B-1b)}$$

$$a = 2\, d_{M1} \sin(\psi_{M1}) + 2\, d_{M2} \sin(\psi_{M2}) \sin[(\pi/6) - \delta_{M2}] \quad \text{(B-2a)}$$
$$b = 3^{1/2}\, d_{M1} \sin(\psi_{M1}) + 2 \cdot 3^{1/2} \cdot d_{M2} \sin(\psi_{M2}) \cos \delta_{M2} \quad \text{(B-2b)}$$

Equation B-1 refers to a geometric homo-octahedral sheet model where each octahedral site has the same bond length d_o and flattening angle ψ. Equation B-2 corresponds to a geometric meso-octahedral sheet model where d_{M1} and d_{M2} are the site-specific M1 and M2 metal-anion bond lengths, ψ_{M1} and ψ_{M2} are the flattening angles of M1 and M2 octahedra, and δ_{M2} is the counter-rotation angle of the M2 octahedra (the M1 octahedra have zero counter-rotation).

To compare actual structural refinement data for the 175 single crystals with predictions from Equations B-1 and B-2, site-specific flattening angles ψ_{M1} and ψ_{M2} were obtained (Hazen and Burnham 1973) from the average octahedral sheet height, h_o, and the average metal-anion bond lengths of each of the M1 and M2 sites, <M1-O> and <M2-O>, as

$$h_o = 2\, c \sin\beta \cdot [1/2 - (O4z + 2 \cdot O3z)/3] \quad \text{(B-3)}$$
$$\psi_{M1} = \arccos[h_o / (2 \cdot \langle M1\text{-}O \rangle)] \quad \text{(B-4a)}$$
$$\psi_{M2} = \arccos[h_o / (2 \cdot \langle M2\text{-}O \rangle)] \quad \text{(B-4b)}$$

where *c* and β are the monoclinic lattice parameters defining the direction along which the T-O-T layers stack, and O3*z* and O4*z* are the *z* fractional atomic coordinates of the O3 and O4 atoms. Note that angular brackets are used for average values: e.g., <A> means the average of A. The values of the counter-rotation angle of a M2 octahedron, δ_{M2}, were calculated in the manner described by Mercier et al. (2005b). The average octahedral bond length, <M-O>, and flattening angle, <ψ>, were obtained using the following relationships:

$$\langle M\text{-}O \rangle = (\langle M1\text{-}O \rangle + 2 \cdot \langle M2\text{-}O \rangle)/3 \quad \text{(B-5)}$$
$$\langle \psi \rangle = (\psi_{M1} + 2\, \psi_{M2})/3 \quad \text{(B-6)}$$

Figure B-1 shows lattice-parameter predictions made for *b* using Equations B-1 and B-2 from the average octahedral site properties of the 175 single-crystal 1*M* polytype *C*2/*m* space group micas, as a function of the observed *b*. As ascertained from the narrow scatter of data points along the 1:1 correspondence solid lines displayed on each graph, geometric homo- and meso-octahedral predictions (*y*-axes) give equally good agreements with the observed *b* lattice parameters (*x*-axes) to within approximately ±0.005 Å. Similar agreements are obtained if *a* is considered instead (Mercier 2003). The notable outlier corresponds to norrishite (Eggleton and Ashley 1989), which exhibits unusual octahedral site distortions that are presumably related to Jahn-Teller effects (Tyrna and Guggenheim 1991; Brigatti and Guggenheim 2002).

Therefore, to the extent that unusual octahedral site distortions such as those acting in norrishite are absent, we conclude that in-plane *a* and *b* lattice parameters

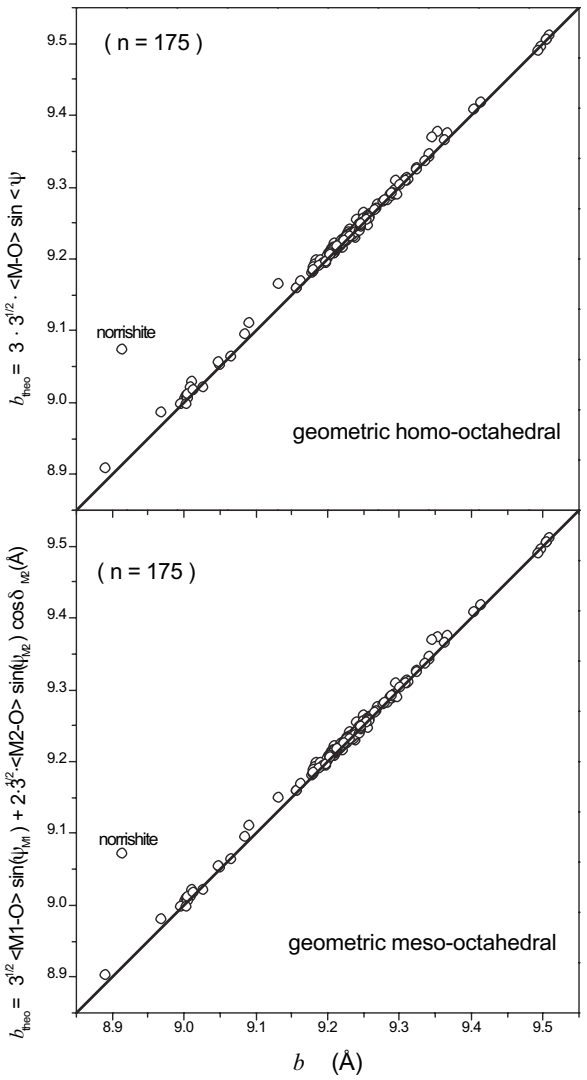

APPENDIX FIGURE B-1. Comparison of observed *b* lattice parameters for the 175 previously published single-crystal 1*M* refinements (*x*-axis) to predictions made using a geometric homo-octahedral (top) and a geometric meso-octahedral (bottom) sheet model via Equations B-1b and B-2b, respectively.

of the 175 single crystals can be adequately predicted (within expected experimental error) using a crystal chemical model involving either geometric homo-octahedral or geometric meso-octahedral sheets, regardless of local distortions (i.e., the individual bond lengths, edge lengths, and bond angles) actually occurring in the M1 and M2 sites.

Tetrahedral sheet

Following Mercier et al. (2005a), three geometric representations can be considered to model the coordination of a given tetrahedral cation *T* with its nearest-neighbor basal oxygen O_{bas} and apical oxygen O_{api} atoms: (1) regular tetrahedron (all T-O bonds are equal and all O-T-O angles are the same); (2) iso-bond-basal-flattened tetrahedron (all T-O bond lengths are equal but the basal flattening angle τ_{bas} of the three O_{bas}-T-O_{bas} angles is allowed to vary); and (3) aniso-bond tetrahedron (the T-O_{api} bond length is not equal to the length of the three T-O_{bas} bonds, and τ_{bas} is allowed to vary). The relationships characterizing these three types of tetrahedra can be written as

$$e_t^{bas} = 2\, d_t^{bas} \sin(\tau_{bas} / 2) \quad \text{(B-7a)}$$

$$h_t^{bas} / d_t^{bas} = [1 - (4/3)\cdot\sin^2(\tau_{bas}/2)]^{1/2} \quad \text{(B-7b)}$$

$$\varepsilon_{bas} = \arccos[2 \sin(\tau_{bas}/2) / (3^{1/2})] \quad \text{(B-7c)}$$

$$\tau_{api} = (\pi/2) + \varepsilon_{bas} \quad \text{(B-7d)}$$

$$h_t = h_t^{bas} + d_t^{api} \quad \text{(B-7e)}$$

$$e_t^{api} = [h_t^2 + (1/3)\cdot(e_t^{bas})^2]^{1/2} \quad \text{(B-7f)}$$

where e_t^{bas} is the length of the three O_{bas}-O_{bas} basal edges, d_t^{bas} is the length of the three T-O_{bas} bonds, τ_{bas} is the value of the three O_{bas}-T-O_{bas} angles, h_t^{bas} is the height of the pyramidal base formed by the three basal T-O_{bas} bonds, ε_{bas} is the angle that a T-O_{bas} bond makes with respect to the basal-oxygen plane, τ_{api} is the value of the three O_{api}-T-O_{bas} angles, h_t is the height of the tetrahedron, and e_t^{api} is the length of the three O_{api}-O_{bas} apical edges.

If a tetrahedral sheet is composed of regular, iso-bond-basal-flattened, or aniso-bond tetrahedra that are linked together in a plane by sharing basal oxygen atoms, then in terms of the tetrahedral basal bond length d_t^{bas} and flattening angle τ_{bas}, the in-plane *a* and *b* lattice parameters are given by (Mercier et al. 2005a):

$$a = 4 \cdot d_t^{bas} \cdot \sin(\tau_{bas}/2) \cdot \cos\alpha \quad \text{(B-8a)}$$

$$b = 4 \cdot 3^{1/2} \cdot d_t^{bas} \cdot \sin(\tau_{bas}/2) \cdot \cos\alpha \quad \text{(B-8b)}$$

where α is the tetrahedral rotation angle (e.g., Donnay et al. 1964a). Note that in these tetrahedral sheet models, there is no tetrahedral tilting or corrugation.

Figures B-2 and B-3 compare geometric crystal chemical model predictions (shown as solid lines) made using Equations B-7 and B-8, respectively, to the following tetrahedral distortion parameters obtained from the single-crystal 1*M* structural refinements: (1) h_t^{bas} is the *euclidian* distance (determined using analytic geometry formulae) between the tetrahedral-site cation (T) and the plane formed by the three basal oxygen atoms (O1, O2, O2') in a given tetrahedron of a given structural refinement of a given sample; (2) <T-O_{bas}> is the average of the three basal bond lengths (<T-O_{bas}> = [(T-O1) + (T-O2) + (T-O2')] / 3); (3) <τ_{bas}> is the average of the three basal O_{bas}-T-O_{bas} angles (<τ_{bas}> = [$\tau_{O1\text{-}T\text{-}O2}$ + $\tau_{O1\text{-}T\text{-}O2'}$ + $\tau_{O2\text{-}T\text{-}O2'}$]/3); and (4) <$\tau_{api}$> is the average of the three apical O_{api}-T-O_{bas} angles (<τ_{api}> = [$\tau_{O3\text{-}T\text{-}O1}$ + $\tau_{O3\text{-}T\text{-}O2}$ + $\tau_{O3\text{-}T\text{-}O2'}$]/3). A remarkable agreement (within expected experimental error) is obtained between experimental observations and predictions in both Figures B-2 and B-3. The only notable exception corresponds again to norrishite (Fig. B-1) and is related to a break of the orthohexagonal $b = 3^{1/2}\cdot a$ relation in this sample (Mercier 2003). In contrast, the latter relation is closely obeyed (within ± 0.005 Å) for all the synthetic powder samples as well as for the remaining 1*M*

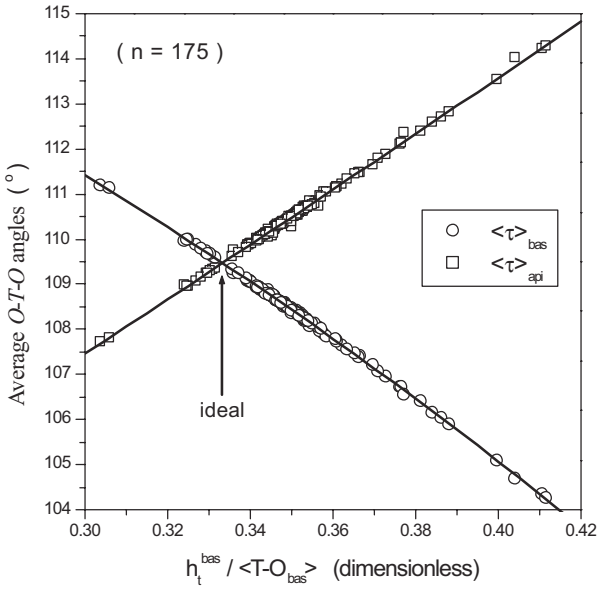

APPENDIX FIGURE B-2. Comparison of geometric crystal chemical model predictions (solid lines) made using Equation B-7 to tetrahedral distortion parameters obtained from the 175 single-crystal 1*M* refinements.

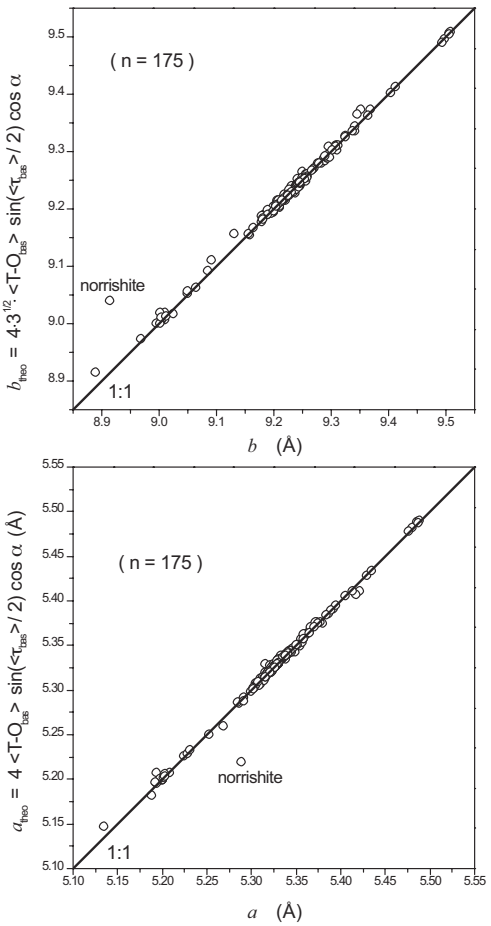

APPENDIX FIGURE B-3. Comparison of observed *a* and *b* lattice parameters for the single-crystal 1*M* refinements to geometric crystal chemical model predictions made using Equation B-8.

single crystals (Mercier 2003), as predicted by the models (see Eqs. B-1, B-2, and B-8). We conclude that geometric crystal chemical models based on tetrahedra with an equal basal bond length d_t^{bas}, a given basal flattening angle τ_{bas}, and a specified rotation angle α, are valid representations of tetrahedra found in micas of 1*M* polytype in *C*2/*m* space group and are sufficient to predict the lateral *a* and *b* extensions of tetrahedral sheets.

Complications arising from octahedral chemical ordering and tetrahedral corrugation

From the perspective of the geometric crystal chemical models used here (Eqs. B-1, B-2, B-7, and B-8), Mercier et al. (2005a) showed that flat tetrahedral sheets having coplanar basal-oxygen atoms, equal basal bond lengths, and tetrahedral apical bonds perpendicular to the **ab**-plane are only possible for geometric homo-octahedral sheet structures. By contrast, geometric meso-octahedral structures must have corrugated tetrahedral sheets where the tetrahedra are required to have unequal basal bond lengths, i.e., (T-O1) ≠ (T-O2) ≠ (T-O2'), and other irregular tetrahedral distortions. Moreover, Mercier et al. (2005b) demonstrated that the 175 single-crystal 1*M* polytype *C*2/*m* space group micas considered here are geometric meso-octahedral (<M1-O> ≠ <M2-O>) whereas the 64 synthetic powder samples are geometric homo-octahedral (<M1-O> = <M2-O>).

In the above two subsections of the present appendix, however, we have shown that the in-plane *a* and *b* lattice parameters of 174 out of the 175 single-crystal 1*M* mica structures can be adequately predicted using simple crystal chemical models that assume either: (1) flat tetrahedral sheets with given values of d_t^{bas}, τ_{bas}, and α; (2) flat geometric homo-octahedral sheets with metal-anion bond length d_o and flattening angle ψ; or (3) flat geometric meso-octahedral sheets with site-specific bond lengths d_{M1} and d_{M2}, flattening angles ψ_{M1} and ψ_{M2}, and a counter-rotation angle δ_{M2} for the M2 octahedra. This means that despite a certain amount of tetrahedral corrugation caused by the geometric meso-octahedral character of the single crystals (Mercier et al. 2005b), one can nonetheless predict *a* and *b* from certain average polyhedral properties in a given structural refinement of a 1*M* polytype *C*2/*m* space group mica.

APPENDIX C. DETERMINATION OF CHARACTERISTIC CATION- AND COORDINATION-SPECIFIC BOND LENGTHS

Assuming that the average cation-anion bond length of a given crystallographically distinct cationic site is a precise measure of the average chemical composition of that site and its coordinating anions, we here adopted an approach where characteristic cation- and coordination-specific bond lengths are used to predict the average bond lengths of the cationic sites in the octahedral and tetrahedral sheets. The resulting cation-specific octahedral and tetrahedral bond lengths used in this work to extract structural information from the lattice parameters of the 64 synthetic powder samples are given in Table 4. Here we explain the procedure used to establish these characteristic cation- and coordination-specific bond lengths.

Octahedral bond lengths

Figure C-1 compares the values of average octahedral sheet bond lengths <M-O> observed for the single-crystal refinements to the following quantities: (1) values of the mean octahedral bond length $\langle d_o \rangle^{Shannon}$ calculated using a set of bond lengths obtained from the tables of ionic radii given by Shannon (1976) (Table 4); and (2) values of the mean octahedral bond length $\langle d_o \rangle^{Weiss}$ calculated

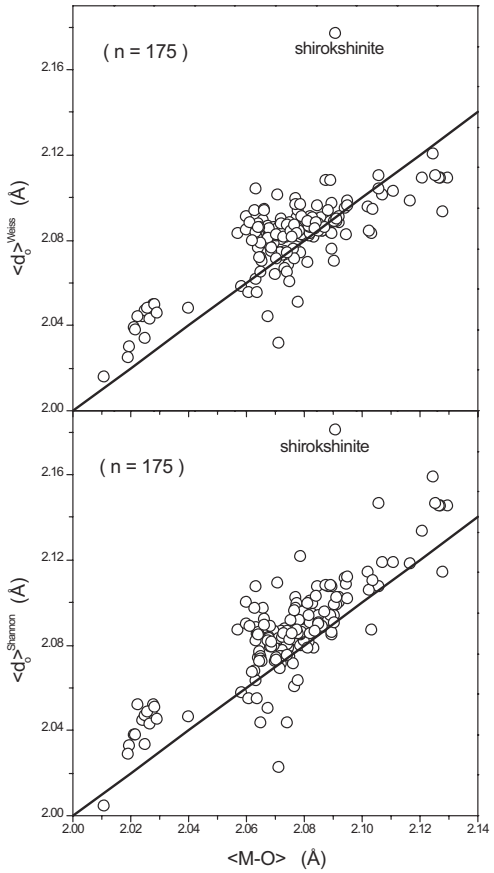

APPENDIX FIGURE C-1. Comparison of the values of average octahedral sheet bond lengths <M-O> observed for the single-crystal 1*M* refinements to values of mean octahedral bond lengths $\langle d_o \rangle^{Weiss}$ and $\langle d_o \rangle^{Shannon}$ calculated from Equation C-1.

using the cation-specific bond distances of Weiss et al. (1992) averaged for *cis* and *trans* occupancies (Table 4).

Values of $<d_o>^{Shannon}$ and $<d_o>^{Weiss}$ were obtained from the chemical compositions reported for each sample as

$$<d_o>^{\text{Shannon or Weiss}} = \Sigma_i\, d_o(M_i) \cdot x_i \quad \text{(C-1)}$$

where (1) the subscript i denotes a particular cation species, (2) $d_o(M_i)$ refers to a cation-specific octahedral bond length; and (3) x_i represents the atomic fraction of cation i contained in the octahedral sites of a given sample. In the calculation of $<d_o>^{Shannon}$, the vacancy bond-length value of Weiss et al. (1992) was taken. Similarly, for $<d_o>^{Weiss}$, the $d_o(M_i)$ values of Shannon (1976) were used if there were no bond lengths provided by Weiss et al. (1992) for given cations.

Values of $d_o(M_i)$ for Weiss et al. (1992) and Shannon (1976) bond lengths are given in Table 4. For comparison, cation-specific M-O distances computed by the bond-valence parameters of Brown and Altermatt (1985) are also presented in Table 4. Note that Shannon (1976) and Brown and Altermatt (1985) cation-specific octahedral bond lengths are equal to within 0.001–0.012 Å. In Figure C-1, the data points display a poor agreement with the 1:1 correspondence solid lines that are shown. Whereas much of the scatter may be related to uncertainties in reported crystal chemical compositions, the main fact that the calculated Weiss et al. (1992) and Shannon (1976) bond lengths are significant overestimates for most samples appears to be robust. A similar poor agreement is observed if the cation-specific $d_o(M_i)$ octahedral bond lengths of Brown and Altermatt (1985) are considered instead (not shown).

Figure C-2 compares the evolutions of the average octahedral bond length <M-O> as a function of $<d_o>^{Shannon}$ for single-crystal structure refinements of: (1) 27 well characterized single-crystal olivine samples with variable chemical compositions in the octahedral sites, $(Ni,Mg,Co,Fe)_2SiO_4$ (Myake et al. 1987; Böstrom 1987; Lager and Meagher 1978; Morimoto et al. 1974; Birle et al. 1968; Smyth 1975; Smyth and Hazen 1973; Rajamani et al. 1975; Hazen 1976, 1977; Nord et al. 1982); and (2) six synthetic single-crystal end-member trioctahedral mica samples having Ni or Co or Mg in the octahedral sheets, $K(Ni,Mg,Co)_3(AlSi_3)O_{10}(OH)_2$ (Redhammer and Roth 2002; Redhammer, unpublished). Single-crystal refinements of biotite-1*M* structures (natural samples) belonging to the [Ann-Phl], aluminous-[Ann-Phl], tetraferri-[Ann-Phl], and oxy-Bt groups are also shown.

Olivine and synthetic (Ni, Mg, Co)-end-member trioctahedral mica samples (Fig. C-2) fall on two distinct lines whose slopes and intercepts differ from those of the 1:1 correspondence solid lines that are shown. Such systematic variations of

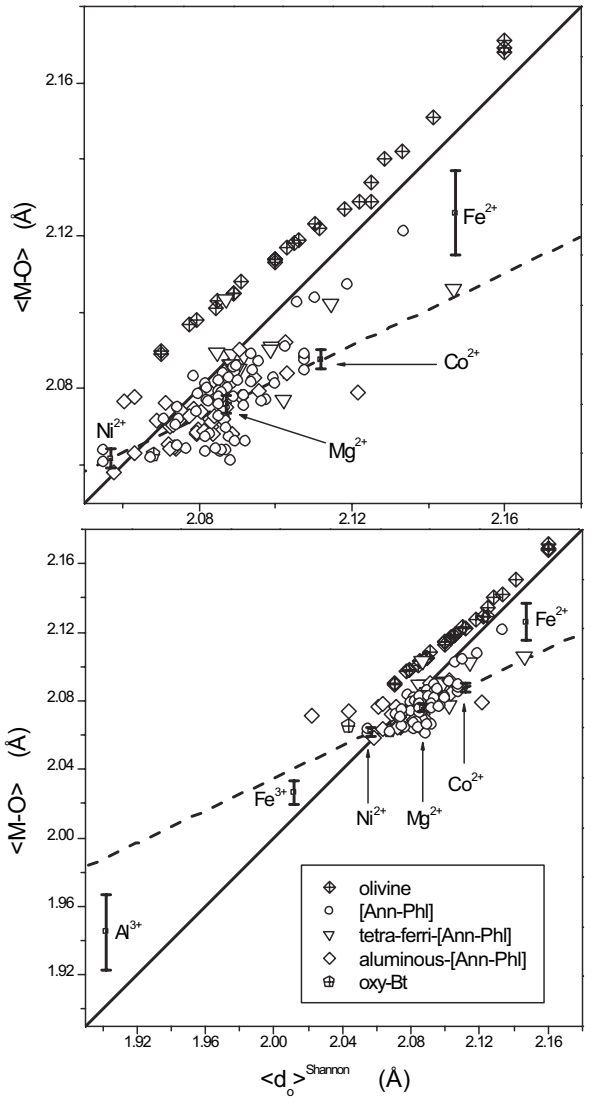

APPENDIX FIGURE C-2. Evolution of <M-O> as a function of $<d_o>^{Shannon}$ for single-crystal structure refinements of selected samples. See text for detailed explanations of the content of this figure.

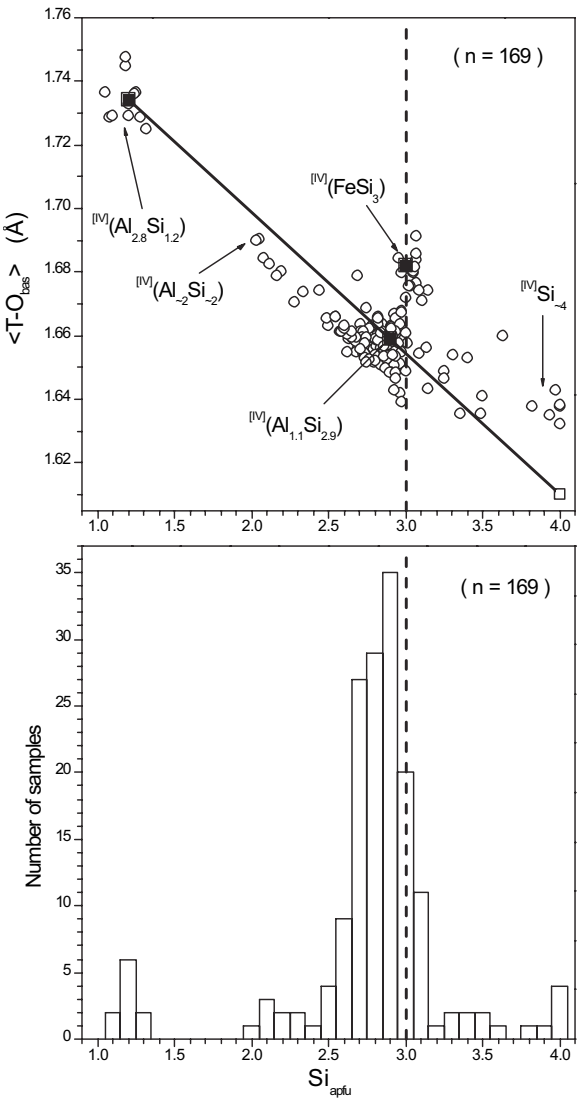

APPENDIX FIGURE C-3. Evolution of $<T\text{-}O_{bas}>$ vs. Si_{apfu} for the single-crystal 1*M* refinements (top), along with the distribution of Si_{apfu} values (bottom). The vertical dashed lines correspond to $Si_{apfu} = 3$.

observed bond lengths with respect to the radii of Shannon (1976) are well known (e.g., Bailey 1984a; Gibbs et al. 1997). In contrast, no clear trend can be discerned for the non-end-member single-crystal biotite-1*M* structures, other than the fact that the cation-specific bond lengths of Shannon (1976) definitively overestimate the mean octahedral bond length in the region between Mg^{2+} and Fe^{2+}, and vice-versa for many samples with an <M-O> size smaller than Mg^{2+}. Given that <M-O> values of well-characterized olivine and end-member mica samples vary linearly, as expected over a small range of average bond lengths, with the $<d_o>^{Shannon}$ values, the scatter observed for the single-crystal biotite-1*M* structures is attributed to uncertainties in the chemical compositions of these samples.

The dashed lines drawn in Figure C-2 correspond to a linear regression through the six single-crystal (Ni, Mg, Co)-end-member trioctahedral mica samples that were used to establish the cation-specific octahedral $d_o(M_i)$ values for Ni^{2+}, Mg^{2+}, and Co^{2+} specified in Table 4. The errors of these cation-specific bond lengths were obtained by linear regression analysis using standard error calculation procedures. In the case of Fe^{2+}, Fe^{3+}, and Al^{3+}, the adopted cation-specific bond lengths are the mid-points between the values predicted by the bond lengths of Shannon (1976) (solid lines) and those yielded by the linear regression described above (dashed lines). The individual errors on these cation-specific bond lengths are estimated by taking half of the difference between two corresponding values for a given cation. The corresponding values are given in Table 4.

Tetrahedra bond lengths

Figure C-3 presents the average basal tetrahedral bond length $<T\text{-}O_{bas}>$ as a function of the reported Si_{apfu} (where X_{apfu} = number of atoms *X* per formula unit), along with the distribution of Si_{apfu} values for the single-crystal samples. In this figure, ~12% of the structures (20 out of 169) have a near-ideal annite-phlogopite Si_{apfu} value of 3. Moreover, there appears to be no simple relationship between $<T\text{-}O_{bas}>$ and Si_{apfu}, presumably due to the fact that the tetrahedral sheets contain not only Si^{4+}, but also other cations such as Al^{3+}, Fe^{3+}, and Ti^{4+}, in differing amounts.

Given the above situation, cation-specific basal tetrahedral bond lengths were determined as follows. In Figure C-3, the black squares represent the $T\text{-}O_{bas}$ distances that were assumed for $^{[IV]}(Al_{1.1}Si_{2.9})$, $^{[IV]}(FeSi_3)$, and $^{[IV]}(Al_{2.8}Si_{1.2})$ tetrahedral sheets (Table 4). The $T\text{-}O_{bas}$ and Si_{apfu} values adopted for $^{[IV]}(Al_{1.1}Si_{2.9})$ and $^{[IV]}(FeSi_3)$ correspond to, respectively: (1) the average $T\text{-}O_{bas}$ value of the six synthetic single-crystal (Ni, Mg, Co)-end-member trioctahedral mica samples referred to above (Redhammer and Roth 2002; Redhammer, unpublished); and (2) the $<T\text{-}O_{bas}>$ value of the synthetic tetra-ferri-annite sample of Donnay et al. (1964b). In the case of $^{[IV]}(Al_{2.8}Si_{1.2})$, the adopted $T\text{-}O_{bas}$ distance corresponds to the average $<T\text{-}O_{bas}>$ and Si_{apfu} values that one obtains from this cluster of samples.

Values of cation-specific basal tetrahedral bond length $d_t^{bas}(T_i)$ were then derived by solving the set of three linear equations given by combining the assumed $T\text{-}O_{bas}$ distances and chemical compositions for $^{[IV]}(Al_{1.1}Si_{2.9})$, $^{[IV]}(FeSi_3)$, and $^{[IV]}(Al_{2.8}Si_{1.2})$ tetrahedral sheets. The values of $d_t^{bas}(T_i)$ hence acquired for Si^{4+}, Al^{3+}, and Fe^{3+} are compiled in Table 4 and the resulting calculated value for $^{[IV]}Si_4$ is shown as an open square in Figure C-3. For comparison, an appropriate set of bond lengths computed from the tables of ionic radii of Shannon (1976) is also presented in Table 4. No error evaluation was attempted for the cation-specific basal tetrahedral bond lengths, but bond lengths consistent with the Shannon (1976) values were also tested.